

แอกทีฟคอนทัวร์เปลี่ยนสเกลได้ในอาณาบริเวณท้องถิ่นโดยใช้เคอร์เนลขยายตัวได้

นายอาเมียร์ ไพศาล

วิทยานิพนธ์นี้เป็นส่วนหนึ่งของการศึกษาตามหลักสูตรปริญญาวิศวกรรมศาสตรมหาบัณฑิต
สาขาวิชาวิศวกรรมไฟฟ้า ภาควิชาวิศวกรรมไฟฟ้า
คณะวิศวกรรมศาสตร์ จุฬาลงกรณ์มหาวิทยาลัย
ปีการศึกษา 2554
ลิขสิทธิ์ของจุฬาลงกรณ์มหาวิทยาลัย

บทคัดย่อและแฟ้มข้อมูลฉบับเต็มของวิทยานิพนธ์ตั้งแต่ปีการศึกษา 2554 ที่ให้บริการในคลังปัญญาจุฬาฯ (CUIR)
เป็นแฟ้มข้อมูลของนิสิตเจ้าของวิทยานิพนธ์ที่ส่งผ่านทางบัณฑิตวิทยาลัย

The abstract and full text of theses from the academic year 2011 in Chulalongkorn University Intellectual Repository(CUIR)
are the thesis authors' files submitted through the Graduate School.

LOCAL REGION-SCALABLE ACTIVE CONTOUR USING EXPANDABLE KERNEL

Mr. Amir Faisal

A Thesis Submitted in Partial Fulfillment of the Requirements
for the Degree of Master of Engineering Program in Electrical Engineering

Department of Electrical Engineering

Faculty of Engineering

Chulalongkorn University

Academic Year 2011

Copyright of Chulalongkorn University

Thesis Title LOCAL REGION-SCALABLE ACTIVE CONTOUR USING EX-
 PANDABLE KERNEL
By Mr. Amir Faisal
Field of Study Electrical Engineering
Thesis Advisor Assistant Professor Charnchai Pluempitiwiriyawej, Ph.D.

Accepted by the Faculty of Engineering, Chulalongkorn University in Partial Fulfillment of
the Requirements for the Master's Degree

..... Dean of the Faculty of Engineering
(Associate Professor Boonsom Lerthirunwong, Dr.Ing.)

THESIS COMMITTEE

..... Chairman
(Associate Professor Chedsada Chinrungrueng, Ph.D.)

..... Thesis Advisor
(Assistant Professor Charnchai Pluempitiwiriyawej, Ph.D.)

..... Examiner
(Assistant Professor Supavadee Aramvith, Ph.D.)

..... External Examiner
(Assistant Professor Surapa Thiemjarus, Ph.D.)

อามีร์ ไฟซาล : แอติฟคอนทัวร์แบบใหม่ที่เปลี่ยนสเกลได้ในอาณาบริเวณท้องถิ่นโดยใช้เคอร์เนลขยายตัวได้ (LOCAL REGION-SCALABLE ACTIVE CONTOUR USING EXPANDABLE KERNEL) อ.ที่ปรึกษาวิทยานิพนธ์หลัก: ดร. ชาญชัย ปลื้มปีติวิริยะเวช, 81 หน้า.

วิทยานิพนธ์นี้เสนอแอติฟคอนทัวร์แบบใหม่ที่เปลี่ยนสเกลได้ในอาณาบริเวณท้องถิ่นโดยใช้เคอร์เนลขยายตัวได้สำหรับการแบ่งส่วนภาพซึ่งเรียกวิธีการนี้ว่า แอล - อาร์ -อี-เค คอนทัวร์แบบจำลองของเราใช้ค่าความเข้มแสงของพิกเซลในเซตของเคอร์เนลที่เปลี่ยนแปลงขนาดได้ที่อยู่ในเส้นคอนทัวร์ เคอร์เนลเหล่านี้จะดึงคอนทัวร์เข้าหาขอบของวัตถุในภาพ คุณลักษณะหลักของแบบจำลองคือขนาดของเคอร์เนลจะค่อยเปลี่ยนแปลงขนาดเพิ่มขึ้นจนกระทั่งถึงขอบของวัตถุ ดังนั้น แอล-อาร์-อี-เค คอนทัวร์ของเราอาจจะไปถึงขอบของวัตถุได้เร็วกว่าแอติฟคอนทัวร์อื่นบางตัว ทำการเปรียบเทียบผลของแอล-อาร์-อี-เค กับแอติฟคอนทัวร์แบบอาศัยข้อมูลภาพขอบและอาณาบริเวณที่มีการเสนอมาแล้วนั้นจากผลการทดสอบพบว่าแบบจำลองของเราให้ผลการแบ่งส่วนภาพที่ดีกว่า มากกว่านั้นเรายังดึงข้อได้เปรียบอื่นของการเปลี่ยนแปลงสเกลอาณาบริเวณท้องถิ่นในการเลือกชนิดของขอบของวัตถุ และยังสามารถที่จะทำการแบ่งส่วนภาพขอบของวัตถุได้ทั้งสองชนิดในการวางคอนทัวร์เริ่มต้นเพียงครั้งเดียว วิธีการที่นำเสนอสามารถแบ่งส่วนภาพที่มีสัญญาณรบกวนขอบวัตถุมีความไวโค้ง ไม่มีความต่อเนื่องและเนื้อของวัตถุที่ไม่มีความเป็นเนื้อเดียวกันได้อย่างมีประสิทธิภาพ และมีช่วงของการเคลื่อนที่ที่กว้างและเคลื่อนที่เข้าหาขอบวัตถุอย่างรวดเร็วในขณะที่การใช้วิธีเซตระดับทำให้แบบจำลองของเรามีความยืดหยุ่น กล่าวคือ แอล -อาร์-อี-เค แบบเกาส์เซียนต์ สามารถแบ่งส่วนภาพที่มีขอบภาพไม่คมชัดได้

ภาควิชา :วิศวกรรมไฟฟ้า..... ลายมือชื่อนิสิต

สาขาวิชา :วิศวกรรมไฟฟ้า..... ลายมือชื่อ อ.ที่ปรึกษาวิทยานิพนธ์หลัก.....

ปีการศึกษา :2554.....

5370615121: MAJOR ELECTRICAL ENGINEERING

KEYWORDS: ACTIVE CONTOUR / LEVEL SET / KERNEL / IMAGE SEGMENTATION

AMIR FAISAL : LOCAL REGION-SCALABLE ACTIVE CONTOUR USING EXPAND-
ABLE KERNEL. ADVISOR : ASST. PROF. CHARNCHAI PLUEMPITIWIRIYAJEJ,
Ph.D., 81 pp.

This thesis presents a novel active contour using scalable local regional information on expandable kernel for image segmentation. We call it LREK active contour. Our model uses intensity values of pixels on a set of scalable kernels along evolving contour. These kernels are to direct contour front towards object's boundary within an image domain. Key feature of our model is that scale of the kernels increases gradually until the boundary is detected. So, our LREK may reach the boundary faster than some other methods. We compare performance of our LREK to existing edge and region-based active contour models. Experimental results show more desirable segmentation outcomes of our method. Furthermore, we also extract directional property of scalable local regional information so that it can choose objects of desirable edge's type. In addition to an ability in segmenting two different edge's type objects with only one initial contour, our proposed scheme performs effectively in segmenting noisy, concave boundary, non-uniform, and heterogeneous textures objects with a large capture range and fast convergence. Meanwhile, level set formulation makes our model topologically flexible. Moreover, our Gaussian LREK is able to trace blur or smooth boundary.

Department : Electrical Engineering Student's Signature

Field of Study : Electrical Engineering Advisor's Signature

Academic Year 2011

Acknowledgements

First and foremost, I am very grateful to ALLAH for everything in my life. During my study at the Digital Signal Processing Research Laboratory, Electrical Engineering (EE), Chulalongkorn University (CU), I have had a fortune and pleasure of studying interesting things. I thank my advisor, Assistant Professor Charnchai Pluempitiwiriyawej. It has been a great honour and pleasure to work under his guidance. I acknowledge all comments and feedbacks to my Thesis Committee, Associate Professor Chedsada Chinrungrueng, Assistant Professor Supavadee Aramvith, and Assistant Professor Surapa Thiemjarus. I also benefited from Image Processing Group Weekly Seminar and International School of Engineering (ISE) Biannual Seminar that give a chance to share and discuss my research progress. I greatly appreciated financial support during my study from the JICA project for AUN/SEED-Net. My thanks also goes to the ISE, AUN/SEED-Net, EE staffs, and my friends in the Image Processing Group, the Communication Laboratory in CU, the Indonesian Student Association in Thailand (PERMITHA), the Indonesian Muslim Student Community in Thailand (Ngajikhun), and the Indonesian Muslim Student Community in Bangkok (Ngajikok).

Contents

	Page
Abstract (Thai)	iv
Abstract (English)	v
Acknowledgements	vi
Contents	vii
List of Tables	ix
List of Figures	x
Chapter	
1 Introduction	1
1.1 Importance	1
1.2 Literature Review	2
1.3 Objective	6
1.4 Scope of the Thesis	6
1.5 Research Procedures	7
2 Theory	8
2.1 The Edge-Based Active Contour Models	8
2.1.1 Geodesic Active Contour (GAC)	8
2.2 Region-Based Active Contour Models	12
2.2.1 Global Region-Based Models	12
2.2.1.1 Active Contour Without Edge (ACWE)	13
2.2.2 Global Region-Scalable Models	16
2.2.2.1 Region-Scalable Fitting (RSF) Model	17
2.2.3 Local Region-Scalable Models	18
2.2.3.1 Localizing Region-Based Active Contour (LRAC)	20
2.2.4 Local Region-Based Models	22
2.2.4.1 Active Contour Using Local Regional Information on Extend- able Search Line (LRES)	23
3 Method	26
3.1 Local Region-Scalable Active Contour Using Expandable Kernel (LREK)	26
3.1.1 Scalable Local Regional (SLR) Force	26
3.1.2 Adaptive Local Statistics of Expandable Kernel	30
3.2 Directional LREK (DLREK)	31

Chapter	Page
3.2.1 Evolution Equation	32
3.2.2 Evolution Process	33
4 Experiments	35
4.1 Local Region-Scalable Active Contour Using Expandable Kernel (LREK)	35
4.2 Directional LREK (DLREK)	55
5 Conclusion	59
5.1 Thesis Summary	59
5.2 Discussion	60
5.2.1 Global versus Local Models	60
5.2.2 Effect of Localization to Initialization	60
5.2.3 Relation between Active Contour Models	60
Appendix	67
Appendix A Derivation of the Equation	67
Appendix B List of Publications	69
Biography	70

List of Tables

Table	Page
2.1 Computational cost of the homogeneous circle image.	22
4.1 Computational cost of the synthetic flower image	37
4.2 Computational cost of the synthetic U-shape image.	39
4.3 Computational cost of the air plane image.	40
4.4 Computational cost of the white blood cell image.	41
4.5 Computational cost of the starfish image.	42
4.6 Computational cost of the bear cartoon image.	43
4.7 Computational cost of the T-shape image.	44
4.8 Computational cost of the heterogeneous textures image.	46
4.9 Computational cost of the heterogeneous textures image with salt and pepper noise. . .	47
4.10 Computational cost of the ultrasound image.	48
4.11 Computational cost of the corpus callosum image.	49
4.12 Computational cost of the ventricle image.	51
4.13 Computational cost of the liver tumor image.	52
4.14 Computational cost of the bone image.	53
4.15 Computational cost of the skin image.	55

List of Figures

Figure	Page
2.1 The edge-based active contour models.	8
2.2 Various initial contour placement; (a) outside the object, (b) inside the object, (c) inside and outside the object, and (d) final contour on the object's boundary.	10
2.3 Performance of the GAC on various spatial intensity variation	11
2.4 Various region descriptor of active contour models.	13
2.5 Performance of the ACWE on various spatial intensity variation.	15
2.6 Performance of the ACWE with (a) small and (b) big value of ν on noisy images.	16
2.7 Performance of the RSF on various spatial intensity variation.	18
2.8 Performance of the RSF with (a) small and (b) big value of ν on noisy images.	19
2.9 Performance of the LRAC with various radius on various grayscale intensity image.	20
2.10 Performance of the LRAC on various spatial intensity variation.	21
2.11 Performance of the LRES on various spatial intensity variation.	24
3.1 Scalable local region on expandable kernel.	26
3.2 Flowchart of our LREK evolution process.	30
3.3 Flow chart of our DLREK evolution process.	34
4.1 Performance of several active contour models for a synthetic flower image, i.e., (a) initial, (b) intermediate, (c) final and (d) post-final contour	36
4.2 Performance of several active contour models for a synthetic U-shape image, i.e., (a) initial, (b) intermediate, (c) final and (d) post-final contour.	38
4.3 Performance of several active contour models for an air plane image.	40
4.4 Performance of several active contour models for a white blood cell image.	41
4.5 Performance of several active contour models for a starfish image.	42
4.6 Performance of several active contour models for a bear cartoon image.	43
4.7 Performance of several active contour models for a T-shape image.	44
4.8 Performance of several active contour models for a synthetic heterogeneous textures image.	45
4.9 Performance of several active contour models for a synthetic heterogeneous texture image with added salt and pepper noise.	46
4.10 Performance of several active contour models for an ultrasound image.	48
4.11 Performance of several active contour models for a corpus callsum of an MR brain image.	49
4.12 Performance of several active contour models for a left ventricle of cardiac MR image.	50
4.13 Performance of several active contour models for a liver tumor of a CT scan image.	51

Figure	Page
4.14 Performance of several active contour models for a bone part of an X-ray hand image.	53
4.15 Performance of several active contour models for a skin part of an X-ray hand image. .	54
4.16 Performance of our DLREK for an MR brain tumor image	56
4.17 Performance of our DLREK for a CMR left ventricle image	56
4.18 Performance of our DLREK for an ultrasound image of a small baby	57
4.19 Performance of our DLREK for an MR brain tumor image	57

CHAPTER I

INTRODUCTION

1.1 Importance

Image segmentation is one of the ubiquitous tasks in computer vision. It tries to separate an image into distinct and meaningful regions where segmentation outcome shall clearly mark pixel regions according to the image region it represents. Spatial intensity variation can cause changes in the image intensity such that non-uniform or heterogeneous texture occurs. Thus, real scenes and medical images have rise the challenging segmentation tasks. Moreover, the fact that particular images may have several objects of interest, that overlap each other or lie on a complex background appearance, makes them difficult to be distinguished. The segmentation task may be extended not only to separate desirable objects from its background but also from undesired surrounding objects.

Active contour models is one of the models that have been broadly applied to image segmentation. The segmentation process begins with an initial contour that can be obtained automatically or with user interaction. In these models, the basic idea is to evolve the contour driven by the gradient flow which derived from an energy function that represented and solved in a calculus of variations and partial differential equations (PDEs). A general energy function consists of image features and a closed contour that separate the image. This variational method finds a solution via optimization where typically the energy is minimized by deriving its first variation and iteratively evolving the contour. Such that, when a solution is reached, it will be optimum (maximum or minimum) that is when the contour evolution stops at the boundary.

This variational technique of active contour schemes yields several beneficial properties. This optimization problem is easy to understand by simply analysing its mathematical formulation of the energy functional. A variational solution depends on the energy itself where a particular energy minimization framework will produce a similar final outcome of segmentation which does not depend on the choice or heuristics related to the numerical implementation of the energy functional. Furthermore, these schemes can segment the object boundaries with sub-pixel accuracy and a smooth and closed contour as segmentation outcomes which useful for next processing step. Besides, they can simultaneously achieve image smoothing or non-uniform intensity correction. In the noisy environment, an enhancement operation may not be necessary for active contour to

detect the boundaries. Moreover, incorporation of various prior knowledge such as shape, edge, and intensity of the image is allowed in these schemes.

1.2 Literature Review

Since the work of Kass *et al.* [1] in 1988, snakes or active contour models have been used extensively addressing the problem of image segmentation, one of the important tasks in image processing and analysis. The contour moves and evolves towards object boundaries under action of a combination between internal and external forces that formulated in PDEs derived from the energy functional. While the contour's internal force regulates its smoothness during contour evolution, the contour's external force that generated from image features acts as a gravitational field to pull the contour toward the boundary of desired object within the image domain. The image feature may refer to the edge information or regional appearances. Hence, active contour models can be categorized into edge and region-based ones.

The edge-based external force employs local edge information as a clue to find the boundary. Such edge information derived from image gradient is a response of an edge indicator. So that the contour evolution will stop when it arrives at the edges. Classical snake (CS), proposed by Kass *et al.* [1], represents the contour explicitly in a parametric form and employs gradient vector of image's edge map. It is known to be unable to extract boundary concavity and to have limited capture range. To overcome these problems, recently many edge-based active contours with various improved external forces [7]-[9] have been proposed. Furthermore, still using image gradient, Casseles *et al.* [3] and Maladi *et al.* [2] independently represent the contour implicitly via level set function. Geodesic active contour [3] also embeds edge information into the level set function. It has been shown by Sethian and Osher [2] in 1988 that the level set method is capable in handling complex topology automatically thus enables the contour to change its topology by splitting and merging. While the advantage of topological flexibilities is not readily accessible in the parametric active contours (PAC) [1], [10], these geometric active contours are able to automatically split and merge in a natural way. Nevertheless, they are generally very sensitive to noise and initial conditions. They often have boundary leakage problems where the object is occluded or has weak boundaries.

The region-based external force, as opposed to the edge-based ones which consider only a few pixels in the image gradient as boundary candidates, uses more global information than just the gradient pixels to drive the contour toward the boundaries. As early as 1989, Mumford and Shah [13] proposed the piecewise smooth model that provides theoretical framework of image segmentation that utilizes global regional information. It is later independently implemented with

the level set method by Tsai *et al.* [14] and Vese and Chan [15]. The Mumford-Shah formulation assumes the regions be smooth and slowly varying; whereas, the Chan-Vese model [17] approximates the regions by two piecewise constant functions which are the constants of intensity average inside and outside evolving contour. Furthermore, Yezzi *et al.* [18] added the regional variances instead of just the mean statistics. Their energy function is optimized when the means on two sides the contour are most different. Michailovich *et al.* [19] utilized the Bhattacharyya difference [20] to minimize the probability density functions both sides the contour. These region-based models use global data fitting function.

Instead of using global fitting energy, Li *et al.* [21] proposed region-scalable fitting (RSF) energy using local window analyzed by Brox and Cremers [22] as a statistical interpretation of the piecewise smooth model [13]. Addressing non-uniform intensity problems, the RSF locally approximates the global image intensities using two scalable intensity fitting functions in either sides of the contour. The fixed-scale Gaussian kernel inside and outside the contour convolve each side image regions, thus, allow approximation of intensity averages at a certain regions scale. The RSF provides choices of the scale from small to large Gaussian sigma, however, it is predetermined and not changing in contour's evolution. Hence, we consider this model as a global region-scalable active contour scheme. Similar schemes [23]-[30] are proposed using local energy measure of kernels or windows.

Lankton and Tannenbaum [31] proposed localizing region-based active contour (LRAC). They addressed heterogeneous textures problem by employing regional intensity statistics within fixed-radius ball masks along the contour and ignoring inhomogeneity that may rise far away. With a predetermined ball radius, however, it has a poor capture range and problem of reaching boundary concavity. Darolti *et al.* [32] proposed local region descriptors for active contour evolutions called the LRD. Addressing real scene situation where global distributions of foreground and background overlap, regional information is computed within square windows centered at active contour. To solve the local minima problem and search for the boundary, they added the balloon force. The additional balloon force, however, limits placement of the initial contour. It actually can be put anywhere but only inside the object. Moreover, it remains unclear that the LRD model is capable of tracing any deep concavity and solving the problem of limited capture range. In contrast to the global region-scalable models where global regional statistics is approached by the kernel in two sides of the contour as region-scalable fitting functions, we consider these two models as local region-scalable active contours where region-scalable statistics are controlled by scale of the local window or ball located at the evolving contour.

Phumeechanya *et al.* [33] proposed active contour using local regional information on

extendable search lines called the LRES. The LRES was inspired by active shape models (ASM) [34] and active contours without edges [17]. While the ASM uses pre-determined fixed length search lines that are perpendicular to the contour front to find the strongest edge pixels, the LRES active contour moves itself using the regional statistics on the search lines that are normal to the contour front. Moreover, to extend the capture range into any concave object part, the length of each LRES search line increases until a suspecting boundary is detected. As a result, this model has various capture ranges on its contour front. It has been shown to perform effectively in segmenting images with heterogeneous textures [33]. Nonetheless, the LRES algorithm is quite time consuming. Even though the long thin LRES's search line is extendable, however, not scalable to the image area. It does not have any choice to mask significantly larger area. Hence, we consider it as a local region-based active contour scheme. Similar schemes proposed [35]-[38].

In summary, the choice of RSF's Gaussian kernel and LRAC's ball mask is preferable to maintain scalability than the LRES's search line. In contrast to the RSF where the region-scalable intensity fittings of the kernel are convolved to all around the image, the LRAC and LRES localize the regional statistics in its ball mask and search line that evenly centered and distributed at the contour, thus, ignore any intensity information outside the masking area. Furthermore, the scalability of the RSF's Gaussian kernel and LRAC's ball mask is controlled priori by a pre-determined sigma and radius from small to large choice of the scale. Their scales, however, do not change throughout the evolution process. In essence, the scalability is manually fixed by a user. Although the RSF uses Gaussian kernel we could not find the role of Gaussian function in the segmented images. In addition, using a fixed-area LRAC's ball, the model has poor convergence into concave boundary and poor capture range.

Nevertheless, particular images may have a complex appearance where exists several objects of interest with various edge's type. This makes the objects difficult to be distinguished since they may overlap each other or lie on a complex background. The previous methods, however, may attract the contour regardless any particular edge's type, thus, lead into wrong edges that may have different direction with respect to the desired boundary. Additional directional information is proposed to pull the contour into the intended edges only.

For instance, Park *et al.* [40] proposed directional snake (DS) by adding gradient directional information into the CS which originally considers only magnitudes of image gradient. By choosing directional parameter either $+1$ or -1 , the DS provides inward or outward gradient direction. Angle between gradient and contour's perpendicular direction is to tell which direction to move. The DS moves only toward edges where the angle is smaller than $\pi/2$. On the other hand, when the contour's normal direction is opposite to the gradient direction, corresponding

force is set to zero. In this manner, the DS does not get attracted to the edges that has opposite direction. Thus, only edges with correct gradient direction participate in the deformation. The DS uses TS's force field which is very sensitive to initialization, has limited capture ranges, and boundary concavity problems. Tang *et al.* [41] added directional information into the gradient vector field (GVF) active contour [7] where its vector field is extended by spatially diffused the image gradient. Directional GVF (DGVF) provides two types of edge map function: positive and negative edge map. Positive edge defines an edge transition from a dark into a bright while negative edge is its opposite. The DGVF's external force is similar to the GVF's excepts computed from chosen directional edge map. The contour shall attract edges from the selected edge map function only. Furthermore, Cheng and Foo [42] modified the GVF into dynamic directional GVF (DDGVF). Unlike the TS, GVF, DS, and DGVF where they utilize a static external force, the DDGVF's force field dynamically changes in the deformation process. The DDGVF's vector field has four components of both positive and negative edge in horizontal and vertical direction. During the deformation, each component is automatically switched driving the contour.

As external force of these directional edge-based approaches is in a form of gradient vector field that derived from the image gradient, although they may guide the contour into the intended object's edges, they basically have several drawbacks associated with their external forces. They are considered to have poor convergence into concave parts, limited capture ranges, boundary leakage problems in weak edges, and also to be very sensitive to noises and initial conditions.

No longer using gradient information, Phumeechanya *et al.* [43] proposed edge's type selectable active contour using local regional information on extendable search line. Formulated in parametric curve, the model uses intensity value along a set of search lines. Each search line is designed to be of adaptive length so that it can navigate the contour front toward the boundary. The difference of means intensity on the search line is employed as an information to automatically select the edge's type during the deformation. Balloon force is to drive the contour away from unintended object. However, it limits initialization to be placed inside or outside object of interest only. Although the search line is extendable, its area does not change much to measure significantly smaller or larger pixel area. It is not scalable to image area thus time consuming. Lack of information caused by inappropriate scale results in there is no force to pull the contour towards the boundary.

Nevertheless, those above methods with additional directional information are formulated in the parametric form where such topological change is not readily accessible. Furthermore, making the PAC robust to noise and initialization, Zimmer and Olivo-Marin [10] use parametric contour and replace the gradient information with the Chan-Vese energy [17]. In the presence

of noises, this model does not require to smooth the image which will smooth the edges too. However, they notice a slight misplacement of the boundary caused by noises. This global region-based PAC does not guarantee detecting the boundary accurately.

1.3 Objective

In this thesis, we propose a novel active contour model using scalable local regional information on expandable kernel for image segmentation. The regional information are localized in kernels by masking them only centered at the contour. In order to maintain the scalability and to search for suspecting boundary, we use magnitude of intensity difference within the kernel to let the scale of these kernels vary itself in the level set evolution. Due to various scale of the kernels that adaptively changes in the evolution process, our LREK may converge to the boundary quickly. Meanwhile, preserving the benefits of local region descriptor, scalable local regional information gives the advantages of an ability to segment desired object with noise, intensity inhomogeneity, and heterogeneous textures with fast convergence. Adaptive local statistics of expandable kernel allows our model tracing boundary concavity with a large capture range. By using Gaussian kernel, our model can trace the smooth or blur boundary, hence, show the effect of Gaussian function in the segmented images. Level set formulation of our model makes our active contour topologically flexible. In addition, to inform particular edge's type objects to attract, directional property of our model is extracted from sign of the means intensity difference. Hence, our active contour is able to choose desirable edge's type objects with the same initialization.

1.4 Scope of the Thesis

1. Study characteristics and performances of existing active contour models available in the literature.
2. Propose an active contour using scalable local regional information on expandable kernel for image segmentation.
3. Extract another benefit of scalable local regional information to select desired edge's type object.
4. Apply these proposed schemes to various real scene and medical images.
5. Study characteristics and performance of the proposed method and provide a comparison with existing active contour models.

1.5 Research Procedures

1. Study relevant literatures.
2. Study characteristics and performances of existing active contour models.
3. Classify existing region descriptors of active contour models based on data fitting terms.
4. Develop a novel active contour model that using local region descriptor.
5. Study characteristics and performance of the proposed method and compare it with existing active contour models.
6. Extract another benefit of our model to select desirable edge's type objects.
7. Apply the proposed schemes to various real scene and medical image.
8. Publish in the international conferences.
9. Write the thesis.

CHAPTER II

THEORY

In snakes or active contour models, segmentation process is started by evolving an initial contour, placed around the object, subject to constraints from an image detecting the boundaries.

2.1 The Edge-Based Active Contour Models

2.1.1 Geodesic Active Contour (GAC)

It has been shown by Caselles *et al.* [3] that geodesic active contour (GAC) is derived from a particular class of classical snakes (CS) [1]. To show its relation, we briefly discuss the CS here. Let $I : \bar{\Omega} \rightarrow \mathbb{R}$ be a given image, $\partial\Omega$ its boundary, and $C(s) : [0, 1] \rightarrow \mathbb{R}^2$ be a parametric curve.

$$\begin{aligned} E_{\text{CS}}(C(s)) &= \int_0^1 [E_{\text{internal}}(C(s)) + E_{\text{external}}(C(s))] ds \\ &= \frac{1}{2} \int_0^1 [\alpha |C'(s)|^2 + \beta |C''(s)|^2 - \lambda |\nabla I(C(s))|^2] ds \end{aligned} \quad (2.1)$$

The first two terms are the internal energy that regulate smoothness of the contour where α and β are positive parameters to weigh the contour's tension and rigidity, respectively. Practically, β is usually zero in order to be second-order discontinuous and contain corners. The third term is the external energy which attracts the contour towards image edges. By minimizing this energy, the evolving contour will stop at the points maxima $|\nabla I|$, supposedly the true boundary, while keep the smoothness of the contour at the boundary.

The GAC considers the rigidity coefficient to be zero ($\beta = 0$) and generalizes the edge indicator part by replacing $-|\nabla I|^2$ with $g(|\nabla I|)^2$. Hence, from the CS's energy function in the 2.1, energy components in the GAC are reduced into two parts, $\frac{1}{2} \int_0^1 [\alpha |C'(s)|^2 + \lambda g(|\nabla I(C(s))|)^2] ds$. A general edge indicator (2.2) is defined by a positive and decreasing function such that

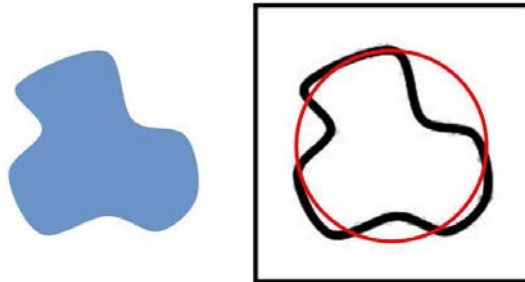


Figure 2.1: The edge-based active contour models.

$\lim_{z \rightarrow \infty} g(z) = 0$. So that, the image would be homogeneous and positive except at the edges which would be zero as illustrated in Figure 2.1. Hence, magnitude of motion forces, $g(|\nabla I|)$, takes smallest values when the evolving contour arrives at the strong edges that exist within the image. In other words, it has an effect to slow down the shrinking or expanding speed once the contour arrives at the edges.

$$g(|\nabla I|) = \frac{1}{1 + |\nabla G_\sigma * I|^p}, p = 1 \text{ or } 2, \quad (2.2)$$

where ∇ is gradient operator and $G_\sigma * I$ is the convolution of the image I with Gaussian smoothing function G_σ .

The GAC represents regularization term of the arclength of the contour as line integral, $L_C = \oint |C'(s)| ds = \oint dr$. A GAC's energy function is obtained by weighting the length element dr with $g(|\nabla I(C(s))|)$, which includes information of object boundaries.

$$E_{\text{GAC}}(C(s)) = \int_0^1 g(\nabla I(C(s))) dr = \int_0^1 g(\nabla I(C(s))) |C'(s)| ds \quad (2.3)$$

This is a computational problem of geodesic or shortest path in a Riemannian space regarding a metric on image edges. By minimizing (2.3), this model not only searches for the path of new shortest length $\oint dr$ but also considers the image features. Thus, GAC evolution equation becomes

$$\frac{\partial C}{\partial t} = g(|\nabla I|) \kappa \vec{\mathcal{N}} - (\nabla g(|\nabla I|) \cdot \vec{\mathcal{N}}) \vec{\mathcal{N}} \quad (2.4)$$

$$\kappa = \text{div} \left(\frac{\nabla \phi}{|\nabla \phi|} \right) \quad (2.5)$$

where κ is the curvature of the contour which has smoothing effect on the contour and $\vec{\mathcal{N}} = -\nabla \phi$ is the inward normal vector.

The GAC also represents the contour implicitly by embedding the contour as the zero level of the level set function where the level set formulation of the GAC is given by

$$\begin{aligned} \frac{\partial \phi}{\partial t} &= |\nabla \phi| \text{div} \left(g(|\nabla I|) \frac{\nabla \phi}{|\nabla \phi|} \right) \\ &= g(|\nabla I|) |\nabla \phi| \text{div} \left(\frac{\nabla \phi}{|\nabla \phi|} \right) + \nabla g(|\nabla I|) \cdot \nabla \phi \end{aligned} \quad (2.6)$$

We see that a gradient term $\nabla g \cdot \nabla \phi$ is naturally incorporated on geodesic framework, however, missing in the CS (2.1) and geometric active contours (2.7). The geometric model that indepen-

dently proposed by Caselles *et al.* [4] and Malladi *et al.* [5] is given by

$$\begin{aligned}\frac{\partial \phi}{\partial t} &= g(|\nabla I|)|\nabla \phi| \operatorname{div} \left(\frac{\nabla \phi}{|\nabla \phi|} \right) + \omega g(|\nabla I|)|\nabla \phi| \\ &= g(|\nabla I|)|\nabla \phi|(\kappa + \omega)\end{aligned}\quad (2.7)$$

where $g(|\nabla I|)$ with $p = 1$ for [5] and $p = 2$ for [4].

The term $\nabla g \cdot \nabla \phi$ in (2.7) drives the contour to object boundaries where ∇g points it exactly into the middle of the boundaries. Because in practice g is never be zero on the edges thus the contour may not stop at the intended boundary. This term is a special help when the boundary has a large variation on its gradient values and it has stronger attraction to locate the contour towards real boundary.

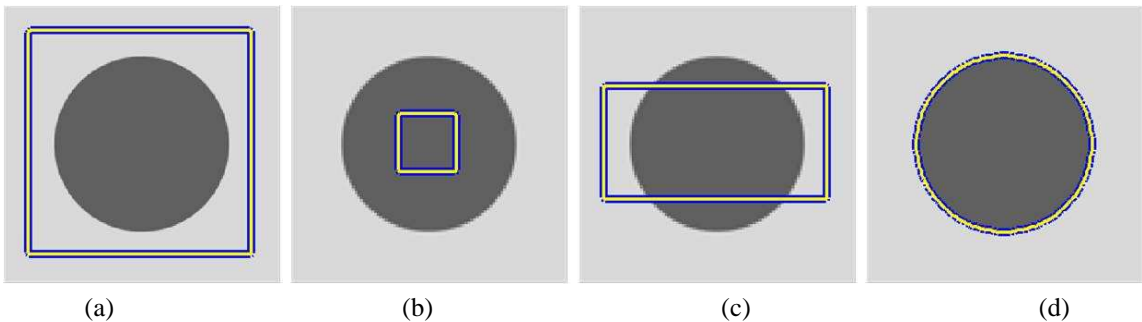


Figure 2.2: Various initial contour placement; (a) outside the object, (b) inside the object, (c) inside and outside the object, and (d) final contour on the object's boundary.

$$\begin{aligned}\frac{\partial \phi}{\partial t} &= g(|\nabla I|)|\nabla \phi| \operatorname{div} \left(\frac{\nabla \phi}{|\nabla \phi|} \right) + \nabla g(|\nabla I|) \cdot \nabla \phi + \omega g(|\nabla I|)|\nabla \phi| \\ &= g(|\nabla I|)|\nabla \phi|(\kappa + \omega) + \nabla g(|\nabla I|) \cdot \nabla \phi.\end{aligned}\quad (2.8)$$

The GAC also adds the balloon force or constant motion term ω similar to the one in the geometrics models in 2.7. It may help to avoid a certain local minima and to increase the convergence speed. On the other hand, removing this term will result in a slower convergence. The term $\omega g(|\nabla I|)|\nabla \phi|$ is also considered as a weighted area constraint where its role is to expand or shrink the contour at a constant speed. Magnitude of this constant velocity determines how fast the contour moves while its sign determines an inward or outward direction it should evolve. This constant which allows to trace concave boundary with a large capture range, on the other hand, introduces an undesired property, i.e., sensitivity to initialization. If the initial contour is entirely outside the object as in Figure 2.2(a), the coefficient ω is to be positive so that the contour moves inward tracing the object. Conversely, if the coefficient ω is set to be negative then the initial

contour need to be put entirely inside the object as in Figure 2.2(b) so that the contour moves outward. If the initial contour is placed both inside and outside the object as in Figure 2.2(c), then the constant ω should be removed so that it can move inward and outward simultaneously, however, with a slower convergence. All these conditions make this model sensitive to initial contour placement.

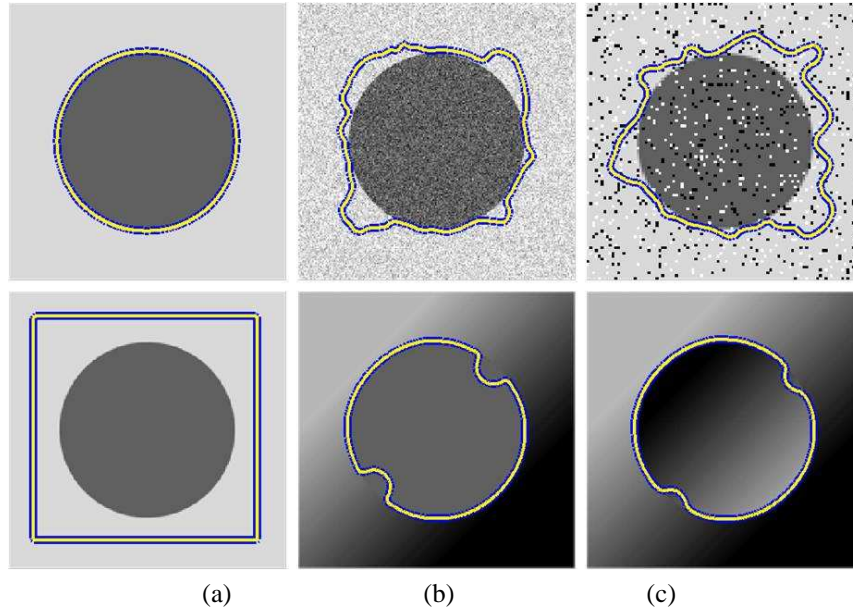


Figure 2.3: Performance of the GAC on various spatial intensity variation

All of these methods rely on the edge indicator depending on the image gradient $|\nabla I|$. Consequently, they can detect only object boundaries defined by the gradient where the edge is assumed located at rapid intensity changes area. In fact, it may not only represent the boundaries but also the noises where the gradient operator may also produce edges of noisy pixels. As a result, the contour may be attracted to wrong edges thus does not arrive at the actual boundary. The first row of Figure 2.3(b) and (c) show the performance of the GAC in the homogeneous intensity image with Gaussian and salt and pepper noise added. To remove the noises, the strength of Gaussian smoothing function need to be high which however would blur the edges as well, or alternatively an enhancement operation need to be performed. These models has been known very sensitive to the noises and initial contour placement. Moreover, in case the object is occluded or has weak boundary, where the edges are not defined well, the contour may pass through the boundary. Nonetheless, an advantage of this model is that there is no consideration of global constraint on the image region inside or outside the contour. So that, even though the object and background are of non-uniform or heterogeneous textures, a correct segmentation may be achieved when strong edge pixels are available. This advantage of the GAC is showed in the second row of Figure 2.3(b) and (c) in handling non-uniform and heterogeneous textures, however, it passes over the actual boundaries in the weak edge.

2.2 Region-Based Active Contour Models

In the literature, there have been several region descriptors of active contour models. We categorize them into four main methods based on their data fitting terms or energy measures. They can be differentiated into global, region-scalable, and local data fitting functions. Based on these criterion, the region-based models are classified into global region-based, global region-scalable, local region-scalable, and local region-based active contours as illustrated in Figure 2.4.

These two global fitting models approximate global image intensity which are interior and exterior regions of the contour. While the global region-based models only allow intensity approximation of entire image domain and do not have choice to approximate a smaller region scale. The global region-scalable models provide choices of the scale from local neighbourhood to the full domain to measure the intensity averages at a certain scale. By sliding the fixed-area kernel into image area both sides of the contour, this scalable regional energy measure fits global image intensity.

While the local region-based models are not provided by any scale choice to measure any smaller or larger intensity region, and thus only able to approximate local intensity regions. In the local region-scalable models, its local energy measure has flexibility to approximate intensity average in small or large scale of the kernel that spread on the contour pixels. These two regions of the kernel inside and outside the contour are formed by splitting the kernel with the contour line as two local energy measures to compute samples within interior and exterior region.

In the global region-scalable models, no matter how small or large scale of the kernel is used, they calculate and include all image intensities by convolving the kernel to inner and outer regions of the contour. Hence, the role of kernel scale is to control degree of intensity details to preserve as the segmentation outcome. Small scale would preserve more intensity details while large scale would ignore some intensity details. On the other hand, the local region-scalable models with small scale kernel will only calculate and include local intensities within the kernel while ignoring intensities outside the kernel. With extremely large scale, it would include all image intensities. In these models, hence, the degree of localness or globalness is controlled by the scale of the kernel.

2.2.1 Global Region-Based Models

The global region-based models use more global constraint than just the gradient pixels. The active contour is to segment the image into two regions: the region inside the contour is to be the object and the one outside the contour is to be the background. The piecewise smooth of

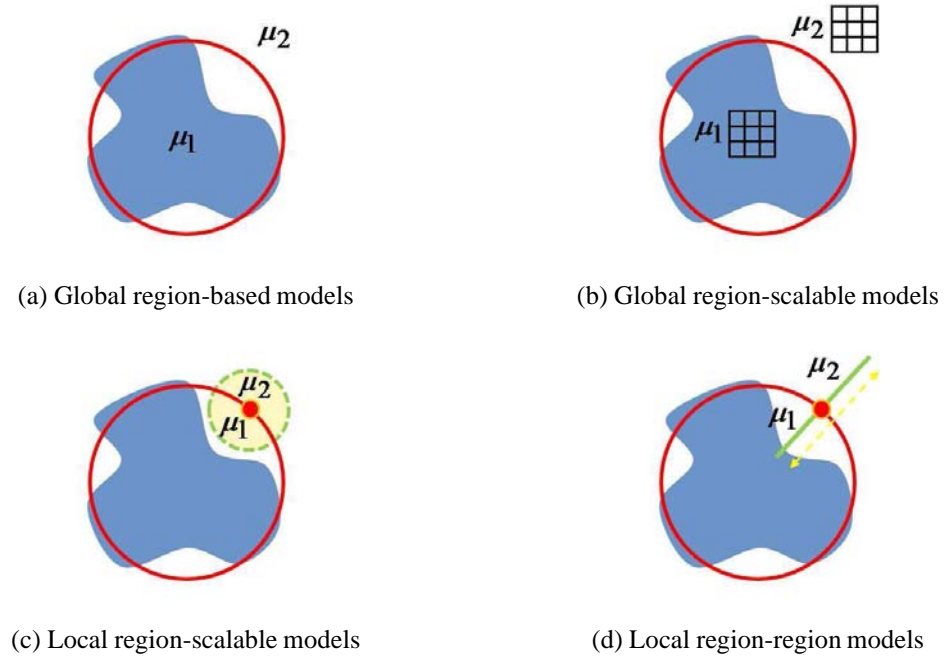


Figure 2.4: Various region descriptor of active contour models.

Mumford-Shah model [13] assumes the two regions be smooth and slowly varying; whereas, the piecewise constant of Chan-Vese model [17] approximates the regions by two constants of intensity averages on two sides of the contour. This energy is minimized when the means optimally approximate the regions. Furthermore, Yezzi *et al.* [13] assume that object and background maximally separate the intensity averages. Their energy is optimized so that the averages inside and outside the contour are most different. Michailovich *et al.* [19] minimize intensity histograms of the interior and exterior regions of the contour.

2.2.1.1 Active Contour Without Edge (ACWE)

Active contour without edge proposed by Chan and Vese [17] is based on simplification of the piecewise smooth of the Mumford-Shah functional. Here are a brief description of the PS model where its energy function is given by

$$E_{\text{PS}}(f, C) = \int_{\Omega} (f(\mathbf{x}) - I(\mathbf{x}))^2 d\mathbf{x} + \rho \int_{\Omega_C} |\nabla f(\mathbf{x})|^2 d\mathbf{x} + \nu |C| \quad (2.9)$$

where $|C|$ is the length of the contour C , ρ , and ν regulate smoothness contributions of the approximating function and of the contour C .

The minimization of the Mumford-Shah functional [13] is obtained with a piecewise smooth function $f(\mathbf{x})$ that approximates the original image $I(\mathbf{x})$ with smooth regions within each connected components in the image domain Ω and discontinuous at the boundaries separated by

an optimal contour C . In practice, however, the PS model involves expensive computation which limits its applications [21].

$$E_{CV}(\mu_1, \mu_2, C) = \sum_{i=1}^2 \lambda_i \int_{\Omega} |I(\mathbf{x}) - \mu_i(\mathbf{x})|^2 d\mathbf{x} + \nu |C| \quad (2.10)$$

A special case of the piecewise smooth (PS) of the Mumford-Shah problem is where the image $f(\mathbf{x})$ in the (2.10) is a piecewise constant function of means intensity $\mu_i(\mathbf{x})$. This model assumes the image intensities be statistically homogeneous and separates the image into disjoint regions of object and background with approximately piecewise-constant intensities of distinct statistics μ_1 and μ_2 , instead of formed by smooth regions. The level set formulation of Chan-Vese energy is given as follows

$$E_{CV}(\mu_1, \mu_2, \phi) = \sum_{i=1}^2 \lambda_i \int_{\Omega} |I(\mathbf{x}) - \mu_i(\mathbf{x})|^2 H_i^\epsilon(\phi(\mathbf{x})) d\mathbf{x} + \nu \int_{\Omega} \delta_\epsilon(\phi(\mathbf{x})) |\nabla \phi(\mathbf{x})| d\mathbf{x} \quad (2.11)$$

where $H_1^\epsilon(\phi(\mathbf{x})) = H_\epsilon(\phi(\mathbf{x}))$ and $H_2^\epsilon(\phi(\mathbf{x})) = 1 - H_\epsilon(\phi(\mathbf{x}))$. $H_\epsilon(\phi(\mathbf{x}))$ and $\delta_\epsilon(\phi(\mathbf{x}))$ [17],[16] are given by

$$H_\epsilon(\phi(\mathbf{x})) = \frac{1}{2} \left[1 + \frac{2}{\pi} \arctan \left(\frac{\phi(\mathbf{x})}{\epsilon} \right) \right] \quad (2.12)$$

$$\delta_\epsilon(\phi(\mathbf{x})) = H'_\epsilon(\phi(\mathbf{x})) = \frac{1}{\pi} \frac{\epsilon}{\epsilon^2 + \phi^2(\mathbf{x})} \quad (2.13)$$

With the smooth Heaviside function (2.12) and its derivative, a smooth Dirac delta function (2.13), the algorithm computes a global minimizer while (3.2) and (3.3) that also used by the LRAC, the algorithm tends to compute a local minimizer [16]-[17].

From (2.11), we see that the difference between intensity values of a given image I and means intensity each side image region μ_1 and μ_2 act as a gravitational force to evolve the contour. If the contour is outside the object as shown in Figure 2.2(a), the intensity value inside the contour will be different from μ_1 and outside the contour be close to μ_2 , the contour will shrink capturing the object. If the contour is inside the object as in 2.2(b), the intensity values inside the contour will be close to μ_1 while outside the contour will be different from μ_2 . Consequently, the contour will expand capturing the object. If the contour is both inside and outside the object as illustrated in Figure 2.2(c), the intensity value inside and outside contour are respectively far different from μ_1 and μ_2 , and thus the contour will shrink and expand simultaneously. The fitting term will be

minimized when the intensity value inside and outside the contour are close to μ_1 and μ_2 and magnitude of the force is zero which is when the contour is placed on the object as in Figure 2.2(d).

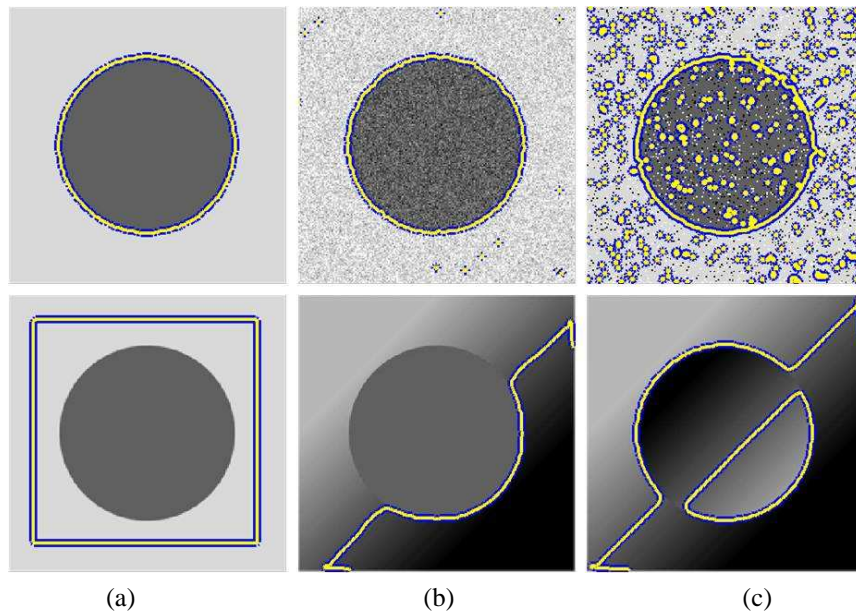


Figure 2.5: Performance of the ACWE on various spatial intensity variation.

By keeping μ_1 and μ_2 fixed and taking the first variation of E_{CV} with respect to ϕ , we obtain the associated Euler-Lagrange equation for ϕ . The energy function is minimized by solving the following gradient flow equation:

$$\begin{aligned} \frac{\partial \phi}{\partial t} &= -(\lambda_1 \delta_\epsilon(\phi) |I - \mu_1|^2 - \lambda_2 \delta_\epsilon(\phi) |I - \mu_2|^2) + \nu \delta_\epsilon(\phi) \operatorname{div} \left(\frac{\nabla \phi}{|\nabla \phi|} \right) \\ &= \delta_\epsilon(\phi) [-\lambda_1 |I - \mu_1|^2 + \lambda_2 |I - \mu_2|^2 + \nu \kappa] \end{aligned} \quad (2.14)$$

$$\mu_i(\mathbf{x}) = \frac{\int_{\Omega} H_i^\epsilon(\phi(\mathbf{x})) I(\mathbf{x}) d\mathbf{x}}{\int_{\Omega} H_i^\epsilon(\phi(\mathbf{x})) d\mathbf{x}}, i = 1, 2 \quad (2.15)$$

where κ is given in (2.5). μ_1 and μ_2 that are given in (2.15) are two constants of means intensity that characterize the intensity of image region inside and outside the contour. Such constants will estimate all samples from two regions either sides of the contour and minimize the global fitting energy. This model is less sensitive to noise as illustrated in the first row of Figure 2.5(b) but such global region descriptor tends to capture not only the object but also white and black pixels of salt and pepper noise in the second row of Figure 2.5(c). Nevertheless, by choosing large value of ν , this model can ignore such small noisy pixels as shown in Figure 2.6 where the first row shows the image corrupted by Gaussian noise while the second row shows the image corrupted by salt and pepper noise. The constants, in fact, can be far away from original image

data if the intensity within inner and outer regions are non-uniform or heterogeneous. This model is applicable to tackle homogeneous intensity images therefore fails to segment particular images with non-uniform and heterogeneous textures which illustrated in the second row of Figure 2.5(b) and (c), respectively.

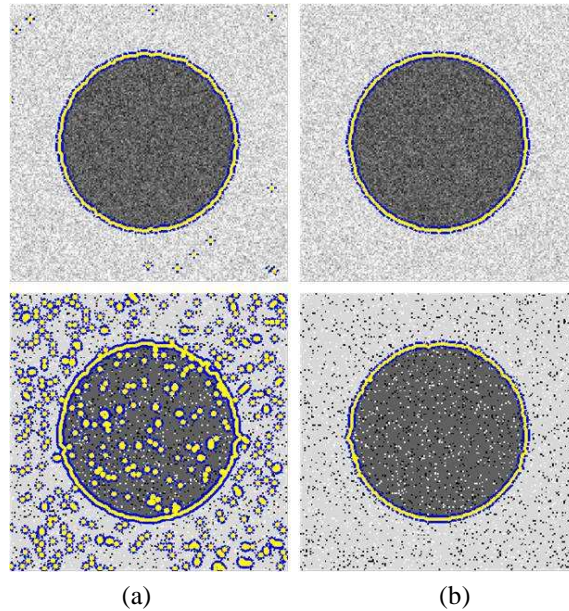


Figure 2.6: Performance of the ACWE with (a) small and (b) big value of ν on noisy images.

2.2.2 Global Region-Scalable Models

Those region-based models actually use global intensity fitting function. In particular images with non-uniform or heterogeneous textures, such global region-based models, however, may not perform efficiently. In cases where the object cannot be distinguished in terms of global statistics, the global region-scalable active contours are capable in dealing intensity inhomogeneity problems. Usage of the kernel, however, leads to drawback of local energy measure. Small scale gives local intensity approximation but results in there is no evolution when it lies entirely on a homogeneous area where local statistics on both side of the contour are the same. By choosing a larger scale, it leads to global intensity approximation and just gives results similar to the global intensity fitting energy. Solving the problem, Piovano and Papadopoulos [24] find optimal scale by comparing the energy measures with a constant threshold. Adaptive local statistics allows the kernel neighbourhood to slowly increase from the minimum scale to the maximum until it crosses the boundary and gives direction where it is supposed to move.

2.2.2.1 Region-Scalable Fitting (RSF) Model

Region-scalable fitting energy proposed by Li *et al.* uses intensity information in local regions with controllable scale which given by

$$E_{\text{RSF}}(\mu_1^K, \mu_2^K, \phi) = \int_{\Omega} \int_{\Omega} \sum_{i=1}^2 \lambda_i K_{\sigma}(\mathbf{x} - \mathbf{y}) |I(\mathbf{x}) - \mu_i(\mathbf{y})|^2 H_i^{\epsilon}(\phi(\mathbf{x})) d\mathbf{x} d\mathbf{y} + \nu \int_{\Omega} \delta_{\epsilon}(\phi(\mathbf{y})) |\nabla \phi(\mathbf{y})| d\mathbf{y} \quad (2.16)$$

where the kernel function $K_{\sigma}(\mathbf{x} - \mathbf{y}) = \frac{1}{2\pi^{\frac{n}{2}} \sigma^n} \exp\left(-\frac{d^2}{2\sigma^2}\right)$ centered at the point \mathbf{x} with a distance d to point \mathbf{y} , the Heaviside and Dirac delta function are respectively given in (2.12) and (2.13), similar to the ACWE, and the μ_1^K and μ_2^K are given in (2.17).

$$\mu_i^K(\mathbf{x}) = \frac{K_{\sigma} * [H_i^{\epsilon}(\phi(\mathbf{x}))I(\mathbf{x})]}{K_{\sigma} * [H_i^{\epsilon}(\phi(\mathbf{x}))]}, i = 1, 2 \quad (2.17)$$

The values of μ_1^K and μ_2^K that minimizes E_{RSF} are weighted means intensity in a neighborhood of \mathbf{x} . They are respectively determined by convolution of $K_{\sigma}(d)$ to inner image region $H_{\epsilon}(\phi(\mathbf{x}))I(\mathbf{x})$ divided by convolution of $K_{\sigma}(d)$ to inner area $H_{\epsilon}(\phi(\mathbf{x}))$ and convolution of $K_{\sigma}(d)$ to outer image region $(1 - H_{\epsilon}(\phi(\mathbf{x})))I(\mathbf{x})$ divided by convolution of $K_{\sigma}(d)$ to outer area $1 - H_{\epsilon}(\phi(\mathbf{x}))$. As a matter of facts, this global region-scalable models can be considered as the global region-based models for $\sigma \rightarrow \infty$.

$$\lim_{\sigma \rightarrow \infty} \mu_i^K(\mathbf{x}) = \frac{\int H_i^{\epsilon}(\phi(\mathbf{x}))I(\mathbf{x})d\mathbf{x}}{\int H_i^{\epsilon}(\phi(\mathbf{x}))d\mathbf{x}}, i = 1, 2 \quad (2.18)$$

In the data fitting term (2.16), each integral is a weighted average square distance from the fitting values $\mu_1^K(\mathbf{x})$ and $\mu_2^K(\mathbf{x})$ to all image regions either side the contour, with the kernel $K_{\sigma}(d)$ as the weight. By convolving the kernel inside and outside the contour, the weighted means characterize the image intensities in an area centered at the point \mathbf{x} whose scale can be controlled by the σ parameter. The data fitting term is region-scalable in a sense that the kernel with a small σ concerns the intensities within a small neighborhood while a large σ exploits a large region of image intensities. With an extremely large σ this model is similar to the global region-based models. This condition is confirmed when $\sigma = \infty$, (2.18) is similar to (2.15) which leads to similarity of this model to the global region-based models behaviours. Hence, the regional scalability allows the choice of the kernel scale to include different scales of intensity information. They can be in a region of any size thus are not restricted only to a small or large region.

By taking the derivative of E_{RSF} with respect to ϕ and keeping μ_1^K and μ_2^K fixed, the

following gradient flow equation is achieved.

$$\begin{aligned} \frac{\partial \phi}{\partial t} &= - \left(\lambda_1 \int_{\Omega} \delta_{\epsilon}(\phi(\mathbf{x})) K_{\sigma} |I - \mu_1^K|^2 d\mathbf{x} - \lambda_2 \int_{\Omega} \delta_{\epsilon}(\phi(\mathbf{x})) K_{\sigma} |I - \mu_2^K|^2 d\mathbf{x} \right) + \nu \delta_{\epsilon}(\phi(\mathbf{y})) \kappa \\ &= \int_{\Omega} \delta_{\epsilon}(\phi(\mathbf{x})) (-\lambda_1 K_{\sigma} |I - \mu_1^K|^2 + \lambda_2 K_{\sigma} |I - \mu_2^K|^2) d\mathbf{x} + \nu \delta_{\epsilon}(\phi(\mathbf{y})) \kappa \end{aligned} \quad (2.19)$$

where κ is as in (2.5).

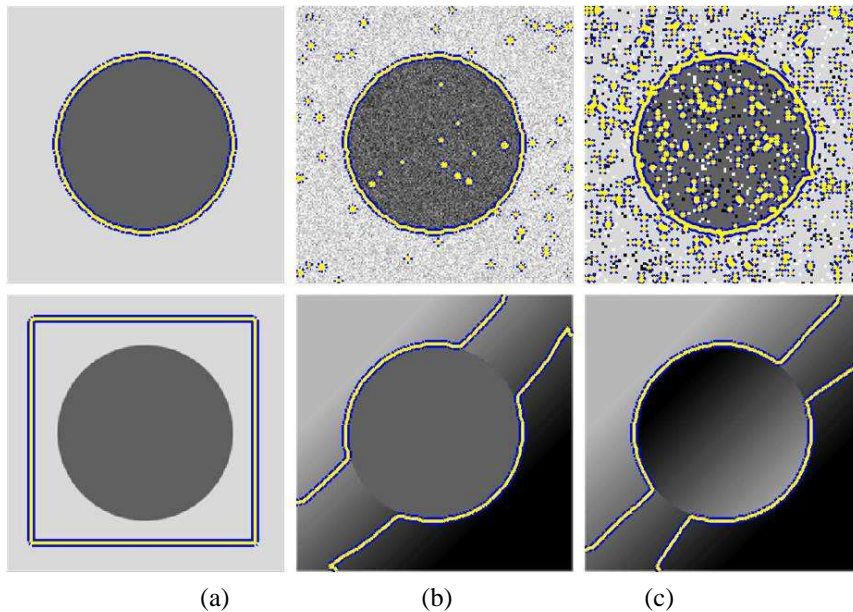


Figure 2.7: Performance of the RSF on various spatial intensity variation.

The values of $\mu_1^K(\mathbf{x})$ and $\mu_2^K(\mathbf{x})$ are determined by all image intensities $I(\mathbf{x})$ in a region centered at \mathbf{x} . For a small displacement $\Delta \mathbf{x}$ from a point \mathbf{x} to an adjacent point $\mathbf{x}' = \mathbf{x} + \Delta \mathbf{x}$, most of the pixels in the region centered at \mathbf{x}' is still on the region centered at \mathbf{x} . Hence, $\mu_1^K(\mathbf{x}')$ and $\mu_2^K(\mathbf{x}')$ are respectively close to $\mu_1^K(\mathbf{x})$ and $\mu_2^K(\mathbf{x})$ due to overlap between neighborhood of \mathbf{x} and \mathbf{x}' . Convolution of a region around \mathbf{x} to the inner and outer image regions of the contour implies the smoothness property. This property therefore overcomes the problem of overlap intensity distribution of the non-uniform or heterogeneous textures as illustrated in the second row of Figure 2.7(b) and (c). Meanwhile, the first row of Figure 2.7(b) and (c) depicts its global computation where it not only captures the object but also the noisy environment. Nonetheless, the noise can be ignored by setting ν parameter to be large as in Figure 2.8.

2.2.3 Local Region-Scalable Models

The LRAC's superiority of localizing regional information to global region one is an ability to handle heterogeneous texture problems. In order to pull the contour towards the boundary, the LRAC masks the intensity statistics within a set of balls with a pre-determined radius along the

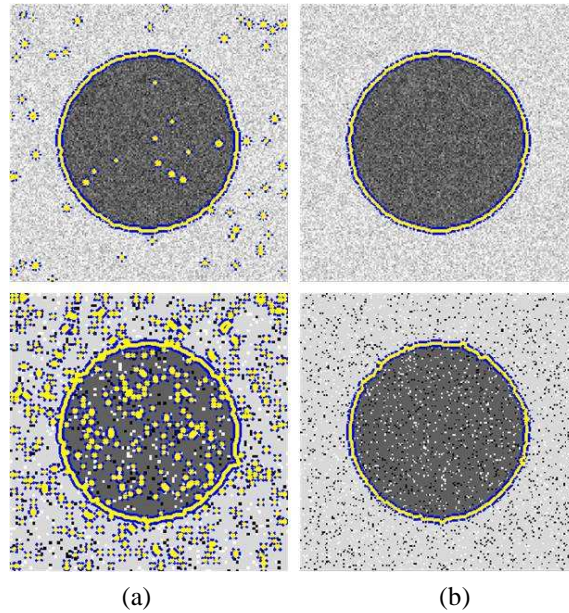


Figure 2.8: Performance of the RSF with (a) small and (b) big value of ν on noisy images.

contour. With a fixed ball radius, the LRAC is unable to trace parts with deep concavity and has poor capture range. Moreover, the user needs to set the radius of the balls priori and wisely, depending on the distance between the position of the initial contour and the location of the object within the image. If the initial contour is placed too far from the boundary and the ball radius is too small, the contour may not reach the boundary or into any concave shapes. In other words, this method may have a diminished capture range. On the other hand, if the radius is set too large, it tends to ignore local intensity details and acts just like the global region-based method. It is difficult to set an appropriate radius, especially when there are objects with various concave shapes. In Figure 2.9, this condition is illustrated with 200×200 pixels size by varying radius of the ball to 10, 20, 30, 40, and 50 pixels and fixing the iteration numbers to 300. Furthermore, the LRD suffers similar problem when the contour lies in a homogeneous region. The local energy measure on both sides of a contour tends to be equal making the motion force approximately zero. Being unable to use information from image parts outside the windows, the contour stuck in a local minimum. An appropriate size of predetermined LRD's windows needs to be chosen wisely. While small windows do not include enough samples to reliably compute statistic forces, large windows are associated with large uncertainty about real boundary positioning. As long as the window size contains enough information from each region and once the boundary is found, the result is influenced minimally and generally accurate. To solve the local minima problem and find the boundary, they added the balloon force to drive the contour to grow when the means and variances of either sides the contour in each window are minimally different. When the contour reaches the boundary, the local regions are different enough for the contour to stop. The additional balloon force, however, limits initial contour placement that it can be put anywhere but only inside

the object of interest. Moreover, it is not clear that the LRD model is capable of tracing any deep concavity and solving the problem of limited capture range.

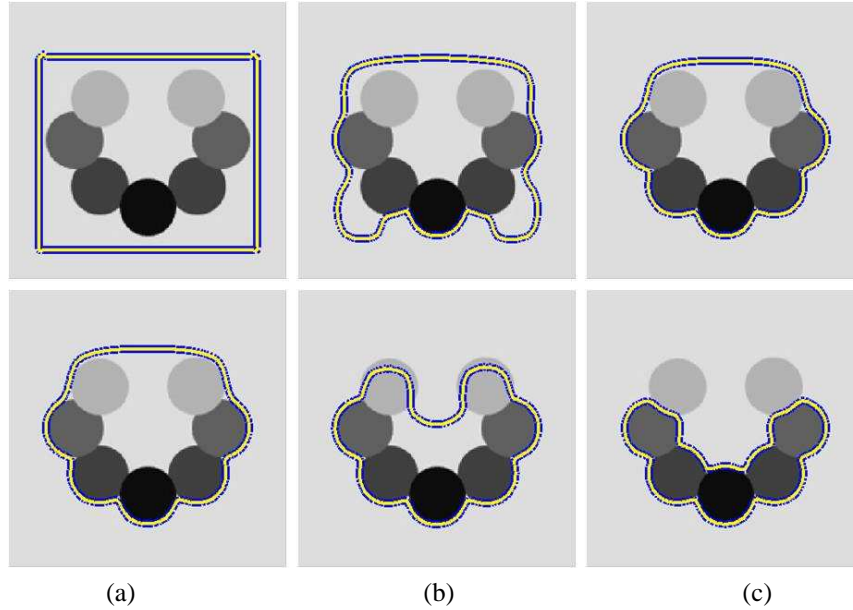


Figure 2.9: Performance of the LRAC with various radius on various grayscale intensity image.

2.2.3.1 Localizing Region-Based Active Contour (LRAC)

Object and background with non-uniform and heterogeneous textures may be correctly segmented with less global information similar to those in the edge-based models. global region descriptors approximate entire image regions however it may not applicable to image with overlapping intensities in non-uniform and heterogeneous textures. When probability densities of image intensities strongly overlap between foreground and background, such piecewise constant function of global region-based models may produce poor segmentation result. To decrease overlapped intensity distribution, the following energy function is re-formulated to sample intensity within regions only around the contour. So, the regions are described only locally to minimize the overlapped intensity. The energy functional proposed by Lankton and Tanenbaum are given by:

$$\begin{aligned}
 E_{\text{LRAC}}(\phi) &= \int_{\Omega} \delta_{\epsilon}(\phi(\mathbf{y})) \sum_{i=1}^2 \int_{\Omega} |I(\mathbf{x}) - \mu_i^B(\mathbf{x})|^2 B(\mathbf{x}, \mathbf{y}) \cdot H_i^{\epsilon}(\phi(\mathbf{x})) d\mathbf{x} d\mathbf{y} \\
 &+ \nu \int_{\Omega} \delta_{\epsilon}(\phi(\mathbf{y})) |\nabla \phi(\mathbf{y})| d\mathbf{y}
 \end{aligned} \tag{2.20}$$

The derivation of the LRAC's energy in (2.20) is computed by replacing $E(\phi)$ with $E(\phi + \xi\psi)$ where ψ represents a small perturbation normal to ϕ weighted by a small number ξ . Thus, the derivative of $E(\phi + \xi\psi)$ is taken with respect to ϕ . The LRAC's gradient flow equation becomes

$$\frac{\partial \phi}{\partial t} = \delta_{\epsilon}(\phi(\mathbf{y})) \left(\int_{\Omega} \delta_{\epsilon}(\phi) B(\mathbf{x}, \mathbf{y}) |I - \mu_1^B|^2 d\mathbf{x} - \int_{\Omega} \delta_{\epsilon}(\phi) B(\mathbf{x}, \mathbf{y}) |I - \mu_2^B|^2 d\mathbf{x} \right) + \nu \delta_{\epsilon}(\phi(\mathbf{y})) \kappa$$

$$= \delta_\epsilon(\phi(\mathbf{y})) \left[\int_\Omega \delta_\epsilon(\phi) B(\mathbf{x}, \mathbf{y}) (|I - \mu_1^B|^2 - |I - \mu_2^B|^2) d\mathbf{x} + \nu \kappa \right] \quad (2.21)$$

$$B(\mathbf{x}, \mathbf{y}) = \begin{cases} 1, & \|\mathbf{x} - \mathbf{y}\| < r \\ 0, & \text{otherwise} \end{cases} \quad (2.22)$$

where $B(\mathbf{x}, \mathbf{y})$ is the ball mask centered on the contour, κ is defined in (2.5), the Heaviside and Dirac delta function are given in (3.2) and (3.3), and μ_1^L and μ_2^L are given as following

$$\mu_i^B(\mathbf{x}) = \frac{B(\mathbf{x}, \mathbf{y}) \cdot H_i^\epsilon(\phi(\mathbf{x})) \cdot I(\mathbf{x})}{B(\mathbf{x}, \mathbf{y}) \cdot H_i^\epsilon(\phi(\mathbf{x}))}, i = 1, 2 \quad (2.23)$$

We can see that behaviour of local and global constraint can be controlled by the radius of the ball. If the ball radius is set to be very small, therefore the LRAC energy function is to be an edge indicator where the pixels within the ball are as small as the width of the edge derived from image gradient. On the other hand, by tuning the radius to be large, the ball will involves the whole image information where the regional statistics are exploited by all pixels in the image.

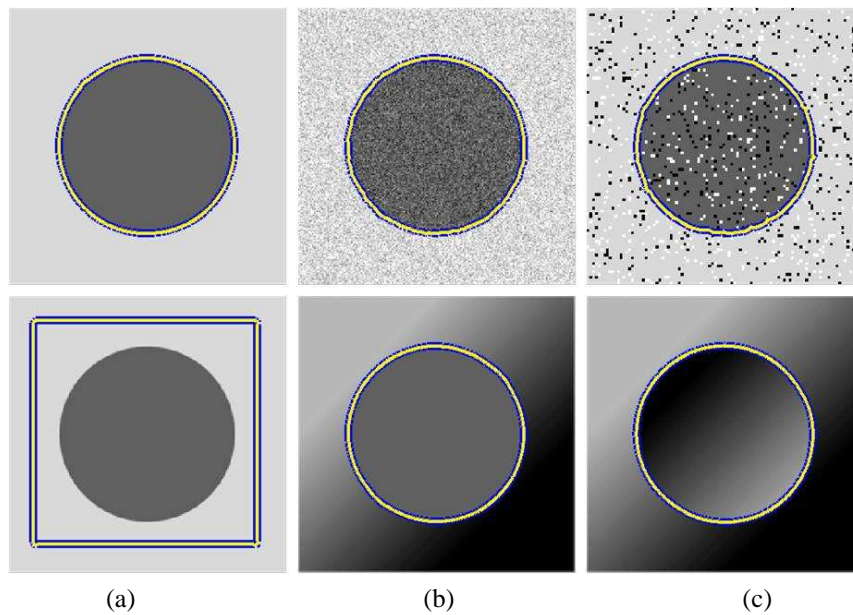


Figure 2.10: Performance of the LRAC on various spatial intensity variation.

Table 2.1 contains computational time required for different size of ball radius of LRAC for image in first row of Figure 2.10(a) which illustrates that the convergence speed is a response of radius size. The smallest radius consumes more and more time to converge and eventually may arrive at a local minimum. Based on less information, the contour makes decision and evolves with a slower convergence. With the largest radius, too global energy measure will make the contour converges quickly however may ignore some intensity details of the object. This shows the trade off between speed of convergence and local radius size. In addition too small or big

Table 2.1: Computational cost of the homogeneous circle image.

Radius (pixels)	Computational Time	
	Iterations	Time (s)
10	810	144.3441
15	310	62.8119
20	155	32.2441
25	95	19.5210
30	75	16.8365
35	70	17.3614
40	70	18.1929
45	70	18.5836
50	70	19.0964

radius may lead to an incorrect segmentation. Nonetheless, it seems the appropriate size of the ball will optimize between the number of iterations and time required for convergence. We see from the Table 2.1 when the radius is getting larger the less time required. After it has reached an optimal radius the number of iterations cannot be reduced any longer while the computational time increases.

2.2.4 Local Region-Based Models

The local region-based method has been shown to effectively segment images with heterogeneous textures (see second line of Figure 2.11(b) and (c)). Also, the first row of Figure 2.10(b) and (c) depicts its robustness to Gaussian and salt and pepper noise. Nevertheless, the LRES forces are determined from a set of long thin search lines where its area is very small compared to the image domain. Therefore, it produces a relatively low force even though it is extendable and spreads on the contour. As a result, the LRES algorithm is quite time consuming where this is confirmed with the Table 2.1 where the smaller area will consume more computational time. Moreover, its inappropriate scale may lack of information to consider, thus, not produce any contour evolution which illustrated in second line of Figure 2.11(b) and (c). Unlike the scalable RSF's Gaussian kernel and LRAC's ball mask, the long thin LRES's search line is not scalable to the image area, thus, does not have any choice to mask significantly larger area even though it is extendable. Using parametric curve, Karaolani *et al.* [35] proposed active contours using finite elements to control local scale. The external force is local regional intensity at fix priori sampled elements along the contour. This local region-based force thus pulls the contour into the boundary. Segmentation accuracy then highly depends on number of the elements. While the LRES has slightly similar idea with this model in embedding local elements in the contour, the authors [36]-[38] embed local energy measure on neighbourhood along both sides of the contour. Ronfard [36] employs intensity of local regions only around the neighbourhood of both sides the contour.

This model, however, requires initial contour placement not too far from the boundary than the neighbourhood width. Dealing with non-uniform image background, J. Mille [37] proposed a narrowband region-based active contour. He calculates two constants of intensity variances within inner and outer narrow region along the contour with fixed thickness. Consequently, it may not have enough capture range and cannot escape a local minima when the energy measure on both regions has similar statistics. Li and Yezzi [38] proposed dual-front active contours. To generate a narrow active region, morphological dilation and erosion are used to extend the contour inside and outside. Although this model is flexible in initializations, suitable width of the active region needs to be priori chosen carefully. Small size leads to local minima problem while large size makes it act with global constraint.

2.2.4.1 Active Contour Using Local Regional Information on Extendable Search Line (LRES)

The LRES active contour uses intensity profiles of the pixels along a set of search lines that are normal to the contour front. These search lines are to inform the contour front which direction to move in order to find object's boundary. The LRES is motivated by ASM the work of Cootes et al where their approach searches for strength edge pixels along a set of predetermined fixed length lines perpendicular to the contour front. Each of these lines guides the contour point to move to a new location where maximum gradient magnitude is located. As a result, this model may have a limited capture range due to fixed length of lines that priori set by a user. Hence, the initial contour must be placed no further far from the object boundary than the length of each search line. Otherwise, the contour front may not move because the lines is too short to find any boundary candidate. In other words, the ASM has limited capture due to fixed length of the lines. To increase the capture range, length of the LRES search lines increases gradually according to the obtained local information within the search lines until a boundary of the object is found. In addition, instead of finding the edge pixel, the LRES uses intensity profile within the search line as criterion to find the boundary.

$$\begin{aligned}
E_{\text{LRES}}(\phi) &= \lambda \int_{\Omega} \delta_{\epsilon}(\phi(\mathbf{y})) \sum_{i=1}^2 \int_{\Omega} |I(\mathbf{x}) - \mu_i^L(\mathbf{y})|^2 L(\mathbf{x}, \mathbf{y}) \cdot H_i^{\epsilon}(\phi(\mathbf{x})) d\mathbf{x} d\mathbf{y} \\
&+ \nu \int_{\Omega} \delta_{\epsilon}(\phi(\mathbf{y})) |\nabla \phi(\mathbf{y})| d\mathbf{y}
\end{aligned} \tag{2.24}$$

The total LRES's energy functional in (2.24) consists of the smoothing term and regional information that is embedded in each search line $L(\mathbf{x}, \mathbf{y})$. The intensity profile along the search line is divided into two regions, one inside the contour and the other outside. μ_1^L and μ_2^L are the

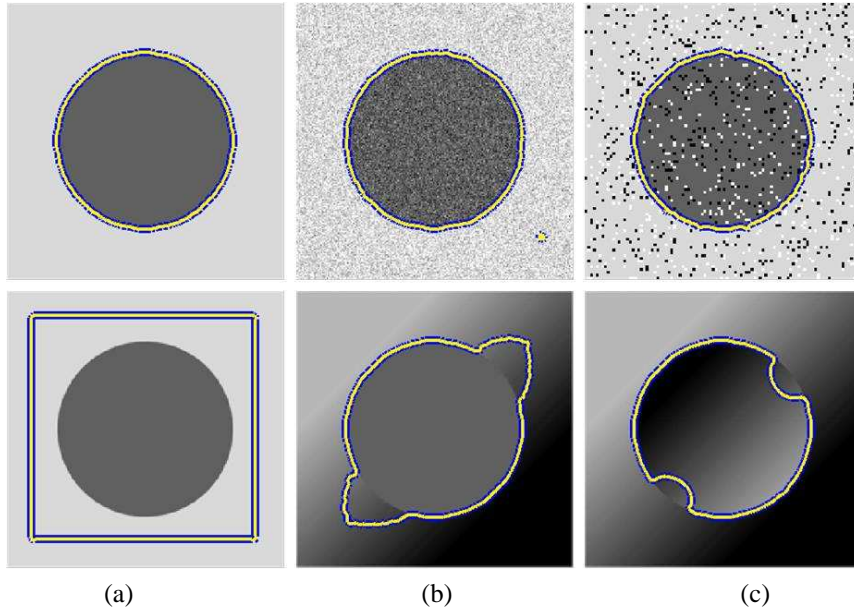


Figure 2.11: Performance of the LRES on various spatial intensity variation.

average statistics calculated from pixel intensity values within the search line that are respectively inside and outside the contour. The search line is spread evenly on the contour according to the number of pixels on the contour. Each search line is gradually extended according to image's local information which informs the contour front which direction to move. The moving direction is determined from the data fitting calculated from the difference between local image intensity I within the search line and respectively μ_1^L and μ_2^L . This energy function will guide the contour front either inward or outward direction. If the intensity value within the search line inside the contour is about the same as μ_1^L and far different from the search line outside the contour, the positive sign of the force will move the contour front inward. On the other hand, if the intensity value outside the contour is closer to μ_2^L than inside the contour to μ_1^L , negative sign of the force will drive the contour front in the outward direction.

By replacing ϕ with $\phi + \xi\psi$, the derivation of the LRES's energy in (2.20) is taken. Thus, $E(\phi + \xi\psi)$ is derived with respect to ϕ where ψ is a small perturbation normal to ϕ weighted by a small number ξ . The LRES's evolution equation is written by

$$\begin{aligned} \frac{\partial \phi}{\partial t} &= \delta_\epsilon(\phi(\mathbf{y})) \left(\int_{\Omega} \delta_\epsilon(\phi)L(\mathbf{x}, \mathbf{y}) |I - \mu_1^L|^2 d\mathbf{x} - \int_{\Omega} \delta_\epsilon(\phi)L(\mathbf{x}, \mathbf{y}) |I - \mu_2^L|^2 d\mathbf{x} \right) + \nu \delta_\epsilon(\phi(\mathbf{y})) \kappa \\ &= \delta_\epsilon(\phi(\mathbf{y})) \left[\int_{\Omega} \delta_\epsilon(\phi)L(\mathbf{x}, \mathbf{y}) (|I - \mu_1^L|^2 - |I - \mu_2^L|^2) d\mathbf{x} + \nu \kappa \right] \end{aligned} \quad (2.25)$$

$$L(\mathbf{x}, \mathbf{y}) = \begin{cases} 1, & (\mathbf{x}, \mathbf{y}) \text{ is on the search line} \\ 0, & \text{otherwise} \end{cases} \quad (2.26)$$

where $L(\mathbf{x}, \mathbf{y})$ is the search line spread on the contour as in, κ is defined in (2.5), the Heaviside and Dirac delta function are respectively given in (3.2) and (3.3), and μ_1^L and μ_2^L are given as following

$$\mu_i(\mathbf{x}) = \frac{L(\mathbf{x}, \mathbf{y}) \cdot H_i^\epsilon(\phi(\mathbf{x})) \cdot I(\mathbf{x})}{L(\mathbf{x}, \mathbf{y}) \cdot H_i^\epsilon(\phi(\mathbf{x}))}, i = 1, 2 \quad (2.27)$$

CHAPTER III

PROPOSED METHODS

3.1 Local Region-Scalable Active Contour Using Expandable Kernel (LREK)

In this chapter, we describe our novel active contour model using scalable local regional information within a set of kernels with various scale. To navigate the contour within image domain towards the boundary, our active contour comprises kernels with various scales. These kernels, centered at the contour front, spread evenly along the contour where its subset are shown in Figure 3.1. The support of each kernel is adaptive throughout the evolution process. The adaptation process of the kernel scale is influenced by image's local information. In other words, each kernel is to be gradually expanded until there is enough information to inform which direction the contour should locally evolve. In this manner, an object located anywhere within the image can be captured, which is opposed to the fixed-area ball mask that produces no evolution when the ball does not cross any object boundary. The expandable kernels allow the contour front to move into any deep concave parts of the object with a large capture range. Meanwhile, scalable local regional information of the kernel enables in segmenting image that has non-uniform and heterogeneous textures with fast convergence.

3.1.1 Scalable Local Regional (SLR) Force

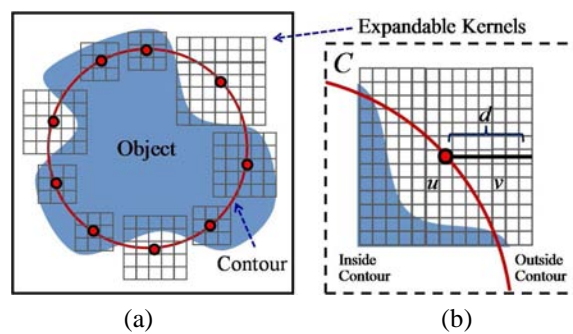


Figure 3.1: Scalable local region on expandable kernel.

The local information that is used in our LREK active contour is the image's weighted average intensity within the kernel, as shown in Figure 3.1 (b). Motion of each pixel on contour front is determined by such scalable local regional information. A contour line divides the kernels into two local regions, one inside the contour and another one outside. Two local regional statistics, μ_{in} and μ_{out} , are the weighted means intensity of all pixels on the inner and outer regions within

the kernel centered on the contour, respectively.

Our model is implemented via level set technique. One of the benefits of this technique is that it can solve problem of required topological changes during evolution. Let a contour $C \subset \Omega$ an image spatial domain, which is embedded as the zero level of the level set function $\phi(\mathbf{x}) : \Omega \rightarrow \mathbb{R}$, where \mathbb{R} is a set of real numbers.

$$C = \{\mathbf{x} \in \Omega : \phi(\mathbf{x}) = 0\} \quad (3.1)$$

where Ω denotes the image domain. In addition, the inner region of the contour, $\phi(\mathbf{x}) > 0$, is defined to be positive where specified in (3.2) by the smoothed Heaviside function $H_\epsilon(\phi)$ [16], [17] and the outer one, $\phi(\mathbf{x}) < 0$, is to be negative which defined by $1 - H_\epsilon(\phi)$. Therefore, the derivative of $H_\epsilon(\phi)$, a smooth Dirac delta function $\delta_\epsilon(\phi)$ as in (3.3), represents the pixels just around the contour C .

$$H_\epsilon(\phi(\mathbf{x})) = \begin{cases} 1 & \text{if } \phi(\mathbf{x}) > \epsilon \\ 0 & \text{if } \phi(\mathbf{x}) < -\epsilon \\ \frac{1}{2} \left[1 + \frac{\phi(\mathbf{x})}{\epsilon} + \frac{1}{\pi} \sin \left(\frac{\pi \phi(\mathbf{x})}{\epsilon} \right) \right] & \text{if } |\phi(\mathbf{x})| \leq \epsilon \end{cases} \quad (3.2)$$

$$\delta_\epsilon(\phi(\mathbf{x})) = \begin{cases} 1 & \text{if } \phi(\mathbf{x}) = \epsilon \\ 0 & \text{if } |\phi(\mathbf{x})| < \epsilon \\ \frac{1}{2\epsilon} \left[1 + \cos \left(\frac{\pi \phi(\mathbf{x})}{\epsilon} \right) \right] & \text{if } |\phi(\mathbf{x})| \leq \epsilon \end{cases} \quad (3.3)$$

Here we derive our local region-scalable force. To mask local region, a kernel is centered and distributed along evolving contour. The kernel function, $K(d)$, is parameterized by point \mathbf{y} that is within a distance, $d = \|\mathbf{x} - \mathbf{y}\|$, with center point at \mathbf{x} which is on the contour, and 0 otherwise. $\|\cdot\|_n$ is the \mathcal{L}_n -norm. A choice of $n = 2$ results in the Euclidean distance while $n = \infty$, the infinite norm, results in a support of square shape as shown in Fig. 1(b). The choice of the kernel is flexible, it can be chosen as a uniform function in (1) similar to the LRAC.

$$K_u(d) = c \quad (3.4)$$

where c is a positive constant.

We also choose a Gaussian kernel in our model. This kernel is considered to be a circle

with different weighting functions. Contribution of the intensity decreases as the distance from the contour or the center point \mathbf{x} to the point \mathbf{y} increases and becomes effectively zero when $d > 3\sigma$.

$$K_G(d) = \frac{1}{(2\pi)^{\frac{n}{2}} \sigma^n} \exp\left(-\frac{d^2}{2\sigma^2}\right) \quad (3.5)$$

We define the SLR energy in each kernel mask, $K(\mathbf{x} - \mathbf{y})$, where \mathbf{y} is any point within image domain with the distance d from center point \mathbf{x} that is exactly on the contour. F only operates on local image information within $K(\mathbf{x} - \mathbf{y})$. The total contribution of the energy is the sum of F values for every $K(\mathbf{x} - \mathbf{y})$ neighborhood distributed on the contour. So, the SLR energy functional of each kernel can be expressed as

$$E_{\text{SLR}}(\phi) = \int_{\Omega} K(\mathbf{x} - \mathbf{y}) \cdot F(I(\mathbf{x}), \phi(\mathbf{x})) d\mathbf{x} \quad (3.6)$$

I denotes the pixel intensity values of a given image. F represents the SLR energy measure at each point along the contour. From existing global region-based models [17]-[19], we mention here at least two candidates for F .

Chan-Vese energy function [17] relies on the assumption that the object and background are statistically homogeneous. This energy is minimized when two constant intensities of their averages approximate the regions optimally, given by

$$F_{\text{CV}} = |I(\mathbf{x}) - \mu_{\text{in}}(\mathbf{y})|^2 H_{\epsilon}(\phi(\mathbf{x})) + |I(\mathbf{x}) - \mu_{\text{out}}(\mathbf{y})|^2 (1 - H_{\epsilon}(\phi(\mathbf{x}))). \quad (3.7)$$

The energy proposed by Yezzi *et al.* [18] is optimized when means intensity of inner and outer regions are well separated. Since it assumes that the means of the object and background are most different. The mean separation energy function is as shown below:

$$F_{\text{MS}} = -\frac{1}{2} |\mu_{\text{in}}(\mathbf{y}) - \mu_{\text{out}}(\mathbf{y})|^2 \quad (3.8)$$

where μ_{in} and μ_{out} represent local intensity averages of the two regions within $K(\mathbf{x} - \mathbf{y})$ located at the contour, written as

$$\mu_{\text{in}}(\mathbf{y}) = \frac{\int_{\Omega} K(\mathbf{x} - \mathbf{y}) H_{\epsilon}(\phi(\mathbf{x})) I(\mathbf{x}) d\mathbf{x}}{\int_{\Omega} K(\mathbf{x} - \mathbf{y}) H_{\epsilon}(\phi(\mathbf{x})) d\mathbf{x}} \quad (3.9)$$

$$\mu_{\text{out}}(\mathbf{y}) = \frac{\int_{\Omega} K(\mathbf{x} - \mathbf{y}) (1 - H_{\epsilon}(\phi(\mathbf{x}))) I(\mathbf{x}) d\mathbf{x}}{\int_{\Omega} K(\mathbf{x} - \mathbf{y}) (1 - H_{\epsilon}(\phi(\mathbf{x}))) d\mathbf{x}}. \quad (3.10)$$

By taking the first variation of (3) with respect to ϕ , we have the following local region-scalable force

$$F_{\text{SLR}} = \int_{\Omega} K(\mathbf{x} - \mathbf{y}) \cdot \frac{\partial F(I(\mathbf{x}), \phi(\mathbf{x}))}{\partial \phi(\mathbf{x})} d\mathbf{x} \quad (3.11)$$

In order to fully express F_{SLR} , we take the derivative of two aforementioned energies, F_{CV} and F_{MS} , with respect to ϕ . $\frac{\partial F(I(\mathbf{x}), \phi(\mathbf{x}))}{\partial \phi(\mathbf{x})}$ becomes

$$\frac{\partial F_{\text{CV}}}{\partial \phi} = \delta_{\epsilon}(\phi(\mathbf{x})) (|I(\mathbf{x}) - \mu_{\text{in}}(\mathbf{y})|^2 - |I(\mathbf{x}) - \mu_{\text{out}}(\mathbf{y})|^2) \quad (3.12)$$

$$\frac{\partial F_{\text{MS}}}{\partial \phi} = -\delta_{\epsilon}(\phi(\mathbf{x})) (\mu_{\text{in}}(\mathbf{y}) - \mu_{\text{out}}(\mathbf{y})) \left(\frac{I(\mathbf{x}) - \mu_{\text{in}}(\mathbf{y})}{A_{\text{in}}} + \frac{I(\mathbf{x}) - \mu_{\text{out}}(\mathbf{y})}{A_{\text{out}}} \right) \quad (3.13)$$

where A_{in} and A_{out} are two areas of a scalable local region of the kernel that split by the contour line, as follows:

$$A_{\text{in}} = \int_{\Omega} K(\mathbf{x} - \mathbf{y}) H_{\epsilon}(\phi(\mathbf{x})) d\mathbf{x} \quad (3.14)$$

$$A_{\text{out}} = \int_{\Omega} K(\mathbf{x} - \mathbf{y}) (1 - H_{\epsilon}(\phi(\mathbf{x}))) d\mathbf{x}. \quad (3.15)$$

$$E(\phi) = - \left(\int_{\Omega} \delta_{\epsilon}(\phi(\mathbf{y})) E_{\text{SLR}} d\mathbf{y} - \nu \int_{\Omega} |\nabla H_{\epsilon}(\phi(\mathbf{y}))| d\mathbf{y} \right) \quad (3.16)$$

We write our total energy term in (3.16). Multiplication of E_{SLR} with the Dirac function $\delta_{\epsilon}(\mathbf{y})$ ensures the contour not to spontaneously develop new contours, although it still allows to solve contour's topological changes. It also accomplishes computation of E_{SLR} only considering pixels contribution within the distance d of the contour and ignores spatial variation that may arise outside of the kernel. In addition, a regularization term is added to regulate contour's elasticity during the evolution by penalizing the arc length of the contour and weighting it by a parameter ν .

$$\frac{\partial \phi}{\partial t}(\mathbf{y}) = \delta_{\epsilon}(\phi(\mathbf{y})) (F_{\text{SLR}} + F_{\text{SM}}) \quad (3.17)$$

$$F_{\text{SM}} = \nu \operatorname{div} \left(\frac{\nabla \phi(\mathbf{y})}{|\nabla \phi(\mathbf{y})|} \right) \quad (3.18)$$

Finally, our LREK evolution equation in (3.17) is obtained by taking the first variation of (3.16) with respect to ϕ where the complete derivation can be found in Appendix A. The first term, F_{SLR} , is our local region-scalable force as in (3.11) that acts as an attractor to move the center of each kernel, which is the contour. The second term as in (3.18) is smoothing force to keep the contour smooth.

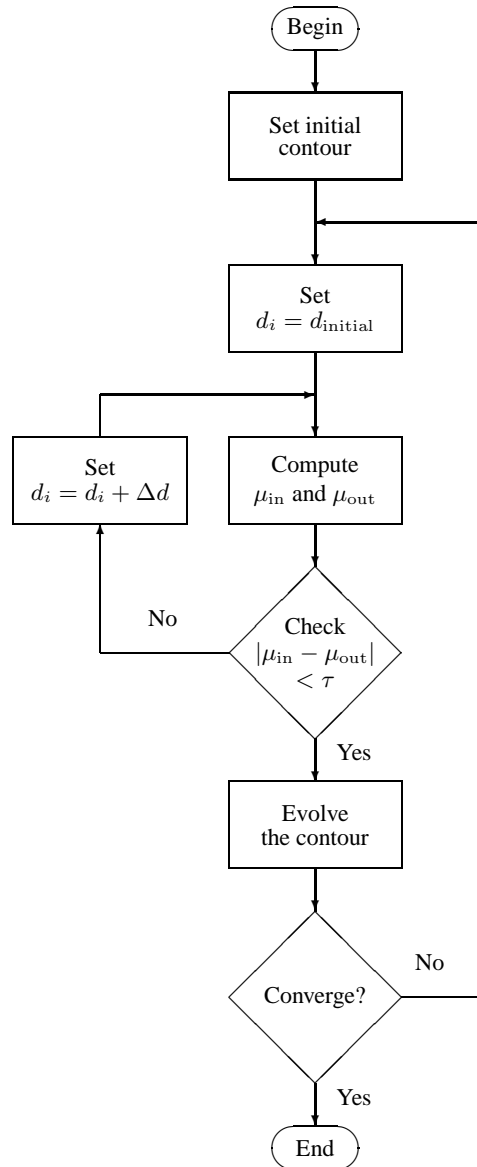


Figure 3.2: Flowchart of our LREK evolution process.

3.1.2 Adaptive Local Statistics of Expandable Kernel

When the fixed-area ball mask lies on a homogeneous region of an object or background, it produces motion force approximately zero. To solve the problem, we are motivated by the local adaptation process. In detecting object's boundary of an image, we let the kernel expand itself until it covers pixels of both object and background. The scale of each kernel, which parameterized by distance d , gradually increases by adding Δd pixels from initial distance d_{start} pixels. This process is allowed by checking whether the kernel overlaps the homogeneous region or not. If it is still on the homogeneous area that means μ_{in} is about the same as μ_{out} . Then, support of the kernel is expanded. Once it has found a non-homogeneous region, supposedly crossing the boundary, there is a significant difference of local regional statistics on either sides of the contour.

In other words, μ_{in} will be of different from μ_{out} . To check how much μ_{in} is different from μ_{out} , their absolute difference is compared to a threshold value τ . While the threshold of the uniform kernel is $[L * \tau]$, where $\tau = [0, 1]$ and $L = 255$ for 8-bit grayscale. For Gaussian kernel, we can conveniently choose the threshold between 0 and 1 since its normalization constant satisfies $\int K_G(\mathbf{x} - \mathbf{y})d\mathbf{x} = 1$. Afterwards, the kernels direct the contour front towards which direction to meet the boundary. The SLR force to evolve the contour either inward or outward depends on the sign of the difference between $|I - \mu_{out}|$ and $|I - \mu_{in}|$. If the intensity profile of the pixel within the kernel I is closer to μ_{out} than μ_{in} , a positive sign of the SLR force will locally move the contour front inward. On the other hand, if the intensity profile of the pixel within the kernel I is about the same as μ_{in} and far different from μ_{out} , a negative sign of the SLR force will drive the contour front in the local outward direction. In addition, magnitude of this force is normalized by taking its sign only. Each force will have value either $-w$ or $+w$, where w is positive parameter. This acts as a force to evolve the contour for one iteration. Another iteration of contour's evolution will be started by initially set $d_i = d_{initial}$ then repeat the kernel adaptation process. The contour's evolution will stop when the contour converges into the boundary. The overall evolution process is illustrated in the flow chart of Figure 3.2.

3.2 Directional LREK (DLREK)

In this section, we extract another advantage of using local region-scalable information that is to select desirable edge's type object. We called it a directional local region-scalable active contour using expandable kernel (DLREK). Our active contour uses variable scale kernel to detect an object's boundary. Scalable local regional information is intensity profile of the pixels within the expandable kernel that spread on the contour. Two means intensity, μ_{in} and μ_{out} , are calculated from inner and outer regions formed by splitting a scalable local region of kernels with the contour. Magnitude of intensity difference is used in detecting object's boundary. It indicates whether the kernel is crossing the boundary or not. If not, it is then expanded. In case it has crossed the boundary, they are used to inform where the contour should locally evolve. However, this attracts the contour towards boundary regardless of any edge's type object. In case the kernel has found unintended edge's type object, the contour point needs to be guided away from such undesired edge by a balloon force. Next, the relationship between μ_{in} and μ_{out} is to be a condition for choosing which object's edges to attract. Sign of its difference is to inform a particular edge's type object to attract. It is used as a switching parameter [43] to manage the forces driving the contour toward objects with desirable edge's type. If μ_{in} is smaller than μ_{out} , it implies that the kernel is lying on a positive edge. Once it crosses a negative edge then μ_{in} will be larger than μ_{out} . With these conditions in mind, we modify LREK evolution equation. In addition to

an ability in looking for objects of desired edge's type with the same initialization, our model preserves many advantages, such as: 1) robustness to noise, 2) an ability to segment non-uniform and heterogeneous textures, 3) a large capture range, 4) an ability to handle boundary concavity, 5) fast convergence, and 6) topologically flexible.

3.2.1 Evolution Equation

Our scalable local regional (SLR) energy is given by (3.6). This energy, however, will guide the contour front towards any type of object's edge. It may not be able to decide particular object's edge to attract. In case the contour lies on an undesired image region, it needs to be guided by another energy. As the third term, we therefore add local balloon energy to locally drive the contour away from the unintended object. Then, we add the switching parameter (3.20) in these two energies so that they will be automatically chosen one in a time. To regulate contour's tension during evolution, we add a smoothing term which associated with contour length as the first term. The second term is our SLR energy. Our total energy becomes

$$\begin{aligned}
 E(\phi) = & \nu \int_{\Omega} \delta_{\epsilon}(\phi(\mathbf{y})) |\nabla \phi(\mathbf{y})| d\mathbf{y} \\
 & + (1 - \alpha) \int_{\Omega} \delta_{\epsilon}(\phi(\mathbf{y})) E_{\text{SLR}} d\mathbf{y} \\
 & + \alpha \int_{\Omega} H_{\epsilon}(\phi(\mathbf{y})) d\mathbf{y}
 \end{aligned} \tag{3.19}$$

$$\alpha = \text{sign}[\beta \cdot \text{sign}(\mu_{\text{in}} - \mu_{\text{out}}) + 1] \tag{3.20}$$

$$\text{sign}(z) = \begin{cases} -1 & \text{for } z < 0 \\ 0 & \text{for } z = 0 \\ +1 & \text{for } z > 0 \end{cases} \tag{3.21}$$

where $H_{\epsilon}(\phi)$ is the smooth regularized Heaviside function and the Dirac delta function $\delta_{\epsilon}(\phi)$ is the derivative of $H_{\epsilon}(\phi)$ as in (3.2) and (3.3), respectively [16], [17]. The switching parameter α automatically manages the SLR and local balloon energy to act in turns regarding local image edge's type. It switches the energy for each kernel at each iteration. Value of α is either 0 or 1. We see that if $\alpha = 0$, E_{SLR} is used and if $\alpha = 1$, then E_{LB} is used. The local image edge's type within the kernel consists of two categories; positive and negative edge's type. Positive edge is where a darker object lies on brighter background and vice versa. The type of object's edge that we are interested in can be chosen by setting edge's type parameter β . Its value is either +1 or -1. If object with positive edge is to be segmented, β is set to be +1 and in case we want to find negative-edge object we just set $\beta = -1$. Moreover, $\text{sign}(\cdot)$ is the sign function where its corresponding value is shown in (3.21). We obtain an evolution equation of (3.22) by taking the

first variation of (3.19) with respect to ϕ .

$$\frac{\partial \phi}{\partial t}(\mathbf{y}) = \delta_{\epsilon}(\phi(\mathbf{y})) [F_{\text{SM}} + (1 - \alpha)F_{\text{SLR}} + \alpha F_{\text{LB}}] \quad (3.22)$$

where F_{SM} and F_{SLR} are given in (3.18) and (3.6), respectively and F_{LB} is as follows

$$F_{\text{LB}} = \begin{cases} +\omega & \text{inward local balloon} \\ -\omega & \text{outward local balloon} \end{cases} \quad (3.23)$$

The first term, F_{SM} , enforces the smoothness of the contour. Secondly, F_{SLR} is our local region-scalable force. Lastly, F_{LB} is the local balloon force, where ω is the positive-valued parameter and acts as the speed-size of F_{LB} . F_{LB} is set to $+\omega$ so that the contour shall locally shrink and vice versa. With this local balloon force, the initialization is not necessarily be placed entirely inside or outside the object of interest. In each kernel at each iteration, either F_{SLR} or F_{LB} will be selected as a force for locally driving the contour point. The SLR force shall pull the contour when local image is of desired edge's type and the local balloon force will locally drive the contour away once it is of undesired edge's type.

3.2.2 Evolution Process

Figure 3.3 depicts the whole evolution process of our model. This process starts by setting initial condition for contour, edge's type parameter, and kernel scale. Next, μ_{in} and μ_{out} are computed for each kernel. Their absolute difference is compared with a threshold value τ . If the difference is less than the threshold then the kernel is expanded. After local adaptation process of expandable kernel found its optimal scale to detect the boundary, we check whether μ_{in} is larger or smaller than μ_{out} . This condition is used in controlling the forces. Supposed we set $\beta = +1$ and found that $\mu_{\text{in}} < \mu_{\text{out}}$, at this time the SLR force drives the contour. Once the kernel found an area with $\mu_{\text{in}} > \mu_{\text{out}}$ then the force on the contour front will be switched into local balloon. For $\beta = -1$, the SLR force pulls the contour to a local region with $\mu_{\text{in}} > \mu_{\text{out}}$. On the other hand, local balloon force shall attract the contour away from a local region with $\mu_{\text{in}} < \mu_{\text{out}}$. The process is repeated until the contour converges.

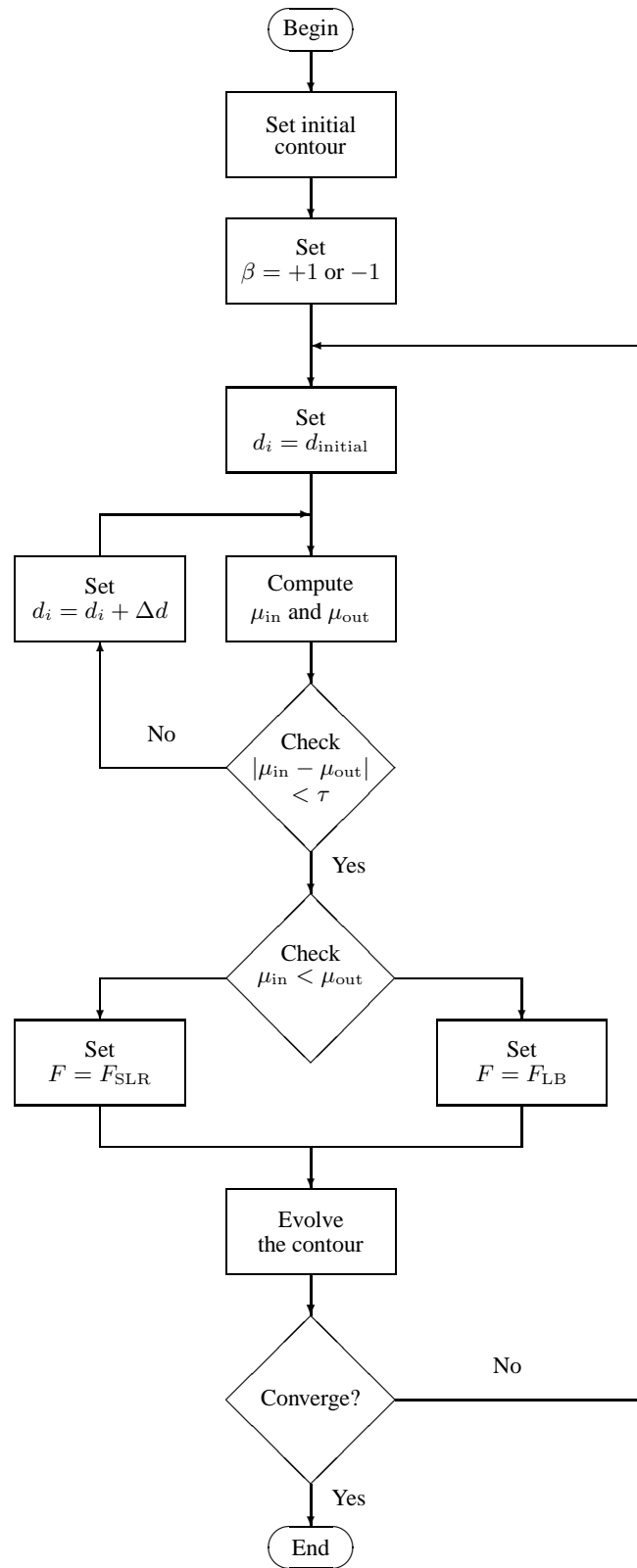


Figure 3.3: Flow chart of our DLREK evolution process.

CHAPTER IV

EXPERIMENTS

4.1 Local Region-Scalable Active Contour Using Expandable Kernel (LREK)

In this section, we performed several experiments to our model proposed in Chapter 3 and various active contour models: the GAC, ACWE, RSF, LRAC and LRES. In all experiment, unless otherwise specified, we set $\omega = 0$ and $\sigma = 1$ for the GAC, $\nu = 0.01 \times 255 \times 255$ and $\lambda_1 = \lambda_2 = 1$ for the ACWE, and $\nu = 0.001 \times 255 \times 255$ and $\lambda_1 = \lambda_2 = 1$ for the RSF, $\nu = 0.8$ for the GAC, LRAC, LRES, and LREK.

Images in Figure 4.1 and 4.2 are arranged into 6 rows and 4 columns. The first to the sixth rows are the GAC, ACWE, RSF, LRAC, LRES, and LREK where each column depicts initial, intermediate, final and post-final contours of each method, respectively.

Figure 4.1 is the synthetic flower image with various grayscale intensities. Table 4.1 shows computational cost of the synthetic flower in the Figure 4.1 for each active contour in two different size of images, i.e., 100×100 and 200×200 pixels. For the image size of 100×100 pixels, the following parameter are used for each model: the GAC with $\omega = 1$, the RSF with $\sigma = 9$, the LRAC with $r = 45$ and F_{CV} , the LRES with $l_{\text{initial}} = 30$, $\Delta l = 5$, and $\tau = 20$, and our LREK with $d_{\text{initial}} = 20$, $\Delta d = 5$, $\tau = 10$, and F_{CV} . For 200×200 pixels image size, each model uses the following parameters: the GAC with $\omega = 3$, the RSF with $\sigma = 15$, the LRAC with $r = 90$ and F_{CV} , the LRES with $l_{\text{initial}} = 60$, $\Delta l = 5$, $\tau = 20$, and our LREK with $d_{\text{initial}} = 40$, $\Delta d = 5$, $\tau = 10$, and F_{CV} .

Intermediate contours for the GAC, ACWE, RSF, LRAC, LRES, and LREK are taken at 30, 2, 4, 85, 100, and 80 iterations, respectively. The GAC, ACWE, RSF, LRAC, LRES, and LREK's contours converge to the boundary at 60, 5, 8, 190, 200, and 160 iterations, respectively. By tuning more numbers of iteration to 90, 7, 8, 275, 300, and 240, their contours remain the same. With $\omega = 1$, the GAC takes 30 and 60 iterations which consume 5.36 and 30.55 seconds, respectively. By setting larger ω , the GAC is able to move faster however will pass through the weak edge. The ACWE and RSF cannot trace boundary of the flower correctly. They exclude circle area inside the flower since its intensity is similar to the background. Even so, the ACWE just require 5 iterations for either size of images with 1.17 and 1.63 second. The RSF needs only 8 iterations for both sizes of images. Its average and total computational cost rise 1.5 times

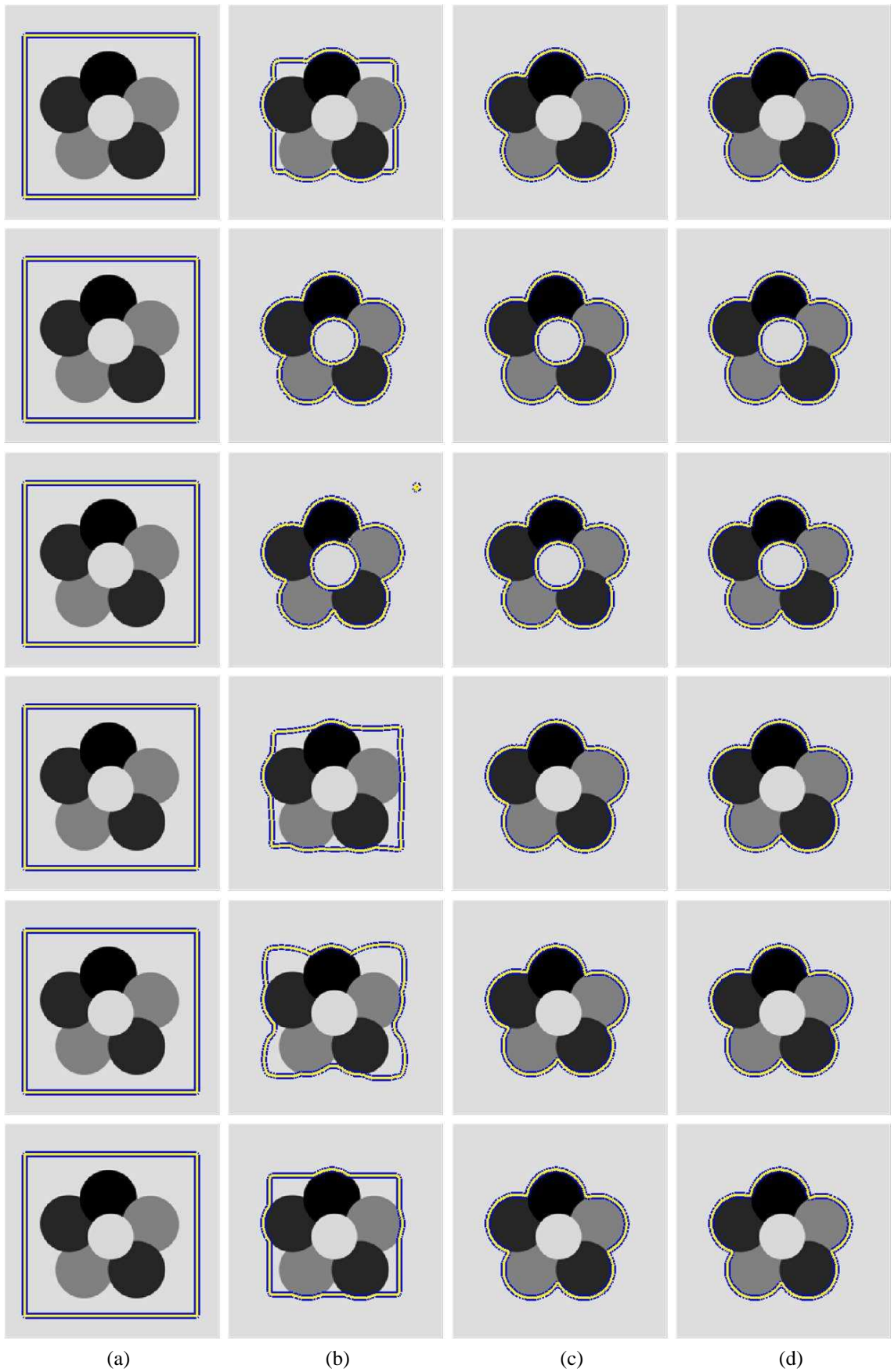


Figure 4.1: Performance of several active contour models for a synthetic flower image, i.e., (a) initial, (b) intermediate, (c) final and (d) post-final contour

from 0.26 to 0.38 second and 2.07 to 3.00 seconds, respectively. With $d = 20$ and $d = 40$, our method converges to desired boundary considerably fast since it just consumes 0.11 and 0.29 second per iteration which rises 2.5 times to the increasing image size. Meanwhile, the LRAC's radius needs to be set as large as 45 and 90 to reach the boundary for both images at 110 and 190 iterations. We observed that its average iteration time increases 4 times from 0.14 to 0.52 second per iteration. With smaller or larger radius than mentioned, the LRAC's contour moves with a slower convergence. Also, it has problem of limited capture range to trace concave shape while it also needs more iteration numbers which consumes more time to capture the object. The larger radius will give fast convergence on the other hand will ignore some intensity details particularly in the weak boundary. The LRES is considered more time consuming than the others. Its total computational cost increases 6.5 times from 161.45 to 1071.71 seconds. This confirms that the long thin search line is not scalable to the image area. Although it can be extended its area does not change much. With the larger and larger image size, its area is still about the same where such a small area of the search line produces a relatively small force in any kind of image size. It requires more and more time to arrive at the boundary. It seems to be more efficient in segmenting image with small size.

Table 4.1: Computational cost of the synthetic flower image

Active Contours	100 × 100 pixels		200 × 200 pixels	
	Iterations	Time (s)	Iterations	Time (s)
GAC	30	5.36	60	30.55
ACWE	5	1.17	5	1.63
RSF	8	2.07	8	3.00
LRAC	110	15.10	190	99.13
LRES	100	161.45	200	1071.71
LREK	85	9.35	160	46.79

Figure 4.2 contains an U-shape image with various grayscale intensities and 200×200 pixels size. For this image, we use following parameter: $\omega = 1$ for the GAC, $\sigma = 5$ for the RSF, $r = 20$ and F_{CV} for the LRAC, $l_{\text{initial}} = 20$, $\Delta l = 5$, and $\tau = 10$ for the LRES, and $d_{\text{initial}} = 20$, $\Delta d = 5$, $\tau = 10$, and F_{CV} for our LREK.

The GAC, ACWE, RSF, LRAC, LRES, and LREK's contour converges at 120, 4, 70, 2000, 360, and 400 iterations, respectively. The intermediate contour in Figure 4.2(b) is taken at 60, 2, 35, 1000, 180, and 200 iterations, respectively. By adding more numbers of iteration to 180, 6, 105, 3000, 540, and 600, each contour does not change. We see that although the ACWE and RSF do not include part of the object that is almost similar to the background intensity their contour

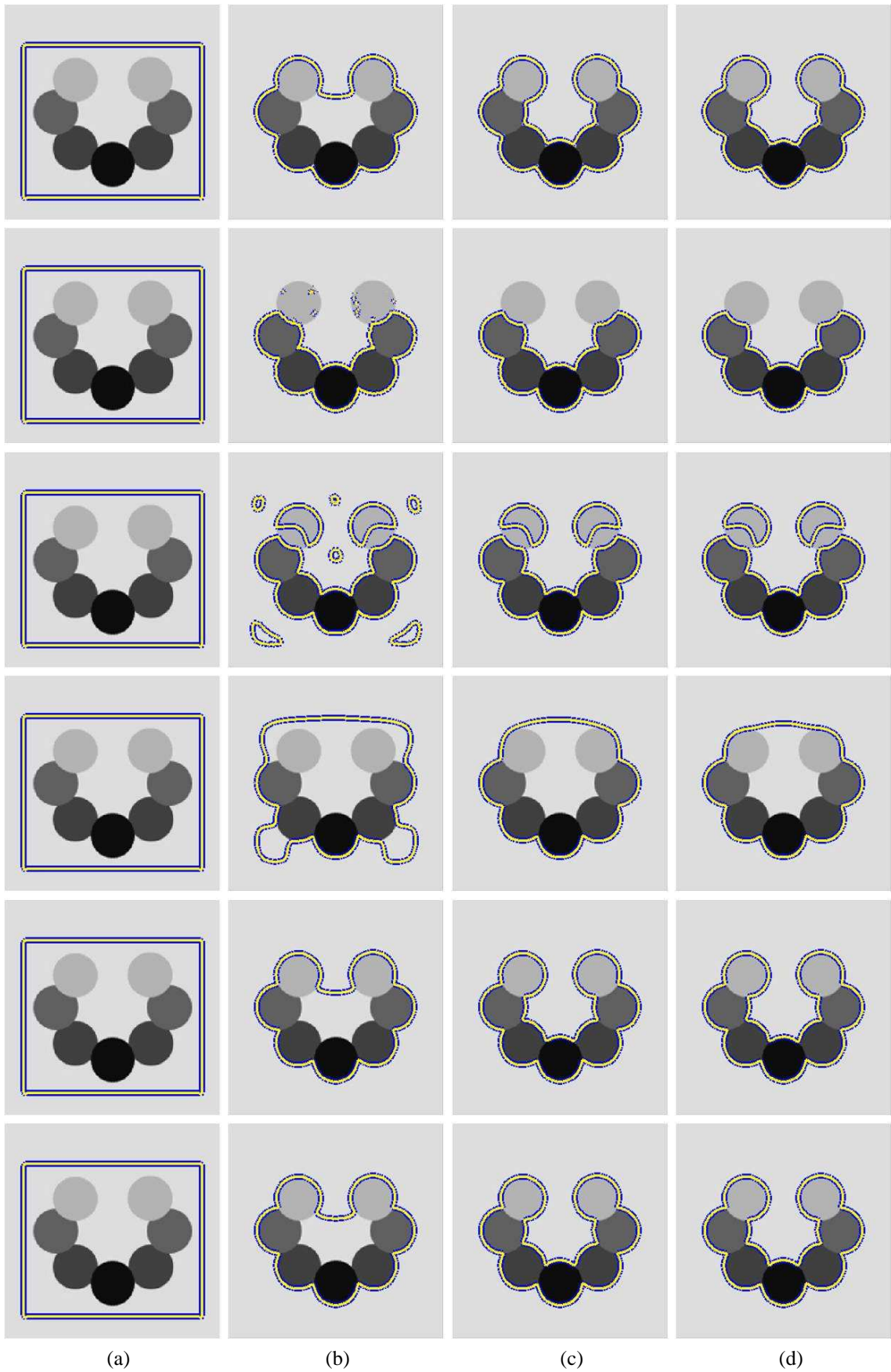


Figure 4.2: Performance of several active contour models for a synthetic U-shape image, i.e., (a) initial, (b) intermediate, (c) final and (d) post-final contour.

Table 4.2: Computational cost of the synthetic U-shape image.

Active Contours	Computational Time		
	Iterations	Time (s)	Average time (s)
GAC	120	121.69	1.02
ACWE	4	1.17	0.29
RSF	70	15.92	0.23
LRAC	2000	356.29	0.18
LRES	360	1008.67	2.80
LREK	400	95.88	0.24

capture the whole object and are distributed everywhere on the image with only small number of iterations. That is because of global computation. It is different to the contour movement of the local models. With the initial contour placed outside the object, the GAC, LRAC, LRES, and LREK's contours gradually shrink tracing the object. With the balloon force $\omega = 1$, the GAC has additional force to move inward with a constant force. At 60 iterations, it has captured the outer part of the object while is trying to move into concave part and finally converges at 120 iterations. Even though, the LRAC's radius is set similar to the LREK's kernel scale which equal to 20 pixels, the LRAC seems to have limited capture range and problem to move into the boundary concavity. At 1000 iterations, its contour is still unable to trace some of the outer part. After 2000 iterations the contour has traced the outer part but does not move inside the concavity. By adding to 3000 iterations, it is still unable to move in. On the other hand, the LRES and LREK's contours are able to move inside where at 180 and 200 iterations their intermediate contours have traced the outer part and are trying to move in. We can see that the GAC, LRES and LREK's contours are placed at about the same intermediate contour position even though they need different numbers of iterations and consume different computational cost. Finally, their contours are placed at the boundary at 120, 360, and 400 iterations by consuming 121.69, 1008.67, and 95.88 seconds, respectively.

In Figures 4.3-4.14, eight images are arranged into two rows and four columns. Images in the first row consist of (a) an original image, segmented image with final contour of (b) the GAC, (c) ACWE, and (d) RSF, respectively. The second row consists of (a) the initial, and final contour of (b) LRAC, (c) LRES, and (d) our LREK that plotted on the image, respectively. Computational cost of each active contour model in segmenting each image are shown in Tables 4.3-4.15 where each table consists of iteration number, computational cost, and average computational time.

Figure 4.3 contains an air plane image with size 200×340 pixels. For this image, we use following parameter: $\sigma = 5$ for the RSF, $r = 15$ and F_{CV} for the LRAC, $l_{\text{initial}} = 25$, $\Delta l = 5$, and $\tau = 30$ for the LRES, and $d_{\text{initial}} = 15$, $\Delta d = 5$, $\tau = 10$, and F_{CV} for our LREK.

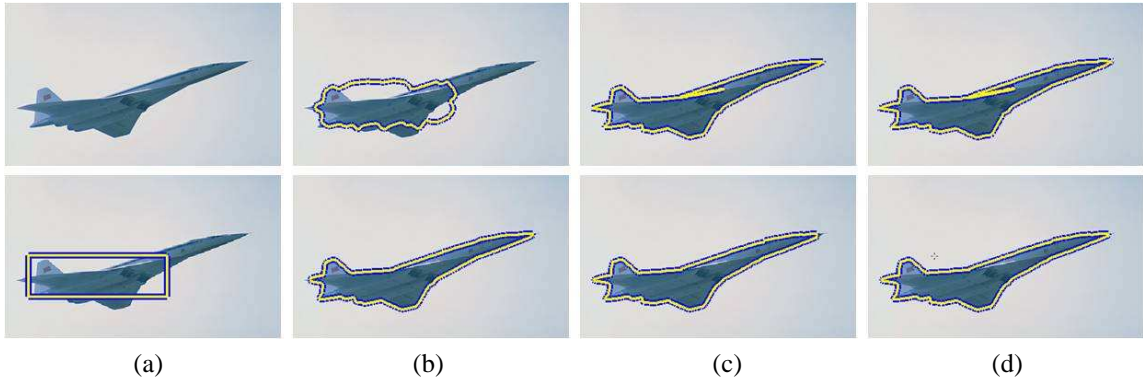


Figure 4.3: Performance of several active contour models for an air plane image.

Table 4.3: Computational cost of the air plane image.

Active Contours	Computational Time		
	Iterations	Time (s)	Average time (s)
GAC	100	103.97	1.04
ACWE	10	6.22	0.62
RSF	20	6.21	0.31
LRAC	1800	281.24	0.16
LRES	500	923.61	1.85
LREK	550	114.94	0.21

We see that all methods are able to segment the air plane image except the GAC. That is due to sensitivity of the GAC to initial condition. We set the balloon force equal to zero since the initial contour is placed both inside and outside the object. However, it seems confused and does not move towards the boundary even after 100 iterations, it is unable to evolve tracing the boundary of the air plane. By choosing the balloon force to be $-\omega$ or $+\omega$, the contour will move faster however it will constantly grow or shrink, respectively. These values are appropriate if the initial contour is placed entirely inside or outside the object. The ACWE and RSF seem to misclassify air plane part where its intensity is similar to the background pixels. Hence, their contours split excluding that pixels. Even so, they converge considerably quick since they only need 10 and 20 iterations with 6.22 and 6.21 seconds, respectively. On the other hand, the LRAC, LREK, and LREK exhibit complete segmentation outcome of the air plane. The LRAC requires more number of iterations with 1800 iterations and 281.24 seconds to converge while the LRES is considered more time consuming since it needs 923.61 seconds for 500 iterations to reach the boundary of the object. Our LREK's contour converges at 550 iterations which only consumes 114.94 seconds.

Figure 4.4 is a white blood cell image of size 200×200 pixels. For this image, we use $\sigma = 49$ for the RSF, $r = 45$ and F_{MS} for the LRAC, $l_{initial} = 40$, $\Delta l = 5$, and $\tau = 30$ for the

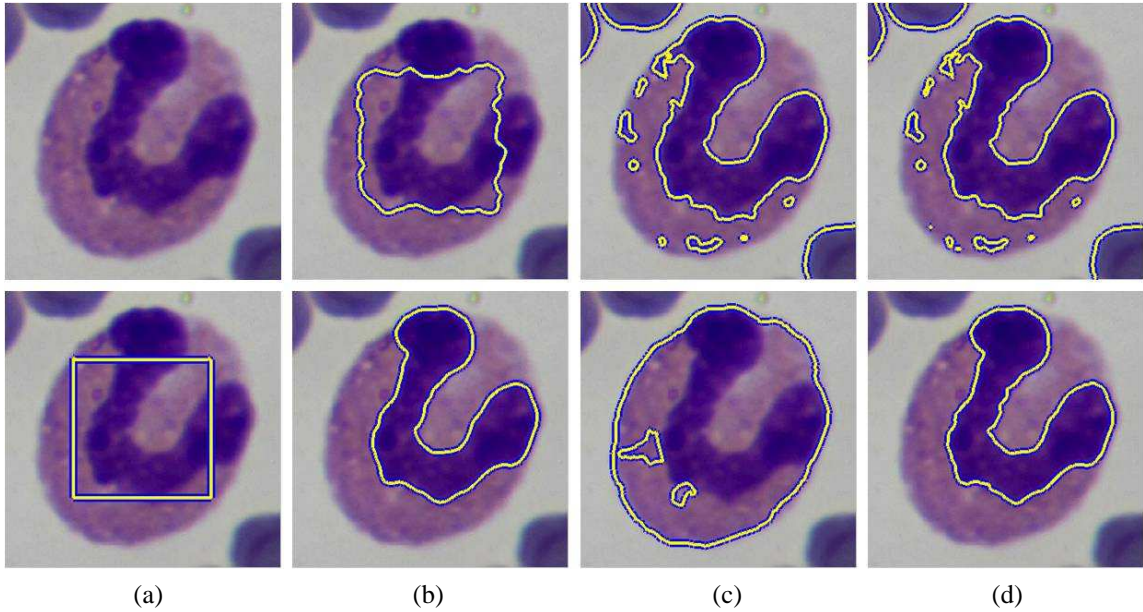


Figure 4.4: Performance of several active contour models for a white blood cell image.

Table 4.4: Computational cost of the white blood cell image.

Active Contours	Computational Time		
	Iterations	Time (s)	Average time (s)
GAC	100	73.23	0.73
ACWE	20	11.63	0.58
RSF	50	69.75	1.40
LRAC	1300	433.52	0.33
LRES	500	2223.21	4.45
LREK	390	141.58	0.36

LRES, $d_{\text{initial}} = 45$, $\Delta d = 5$, $\tau = 20$ and F_{MS} for our LREK.

In Figure 4.4, we intend to trace the U-shape nucleus of the white blood cell. With $\omega = 0$, the GAC evolves slowly and with small capture range. Again, although we set iteration numbers as much as 100, the GAC's contour does not move anywhere. It may also be stuck by noisy environment of the image. We can see that the ACWE and RSF can segment the nucleos, however, they also include some other parts which are not considered as the object. The LRES is segmenting the whole cell instead of the nucleus itself. Meanwhile, it requires expensive computation with 500 iterations for 2223.21 seconds. The LRAC and LREK achieve satisfactory segmentation of the nucleus only while ignoring the other parts. Nonetheless, our LREK converges faster with 390 iterations for 141.58 seconds than the LRAC where consumes 1300 iterations with total computation time 433.52 seconds.

A starfish image in Figure 4.5 has size 200×200 pixels. The parameters are set as follows:

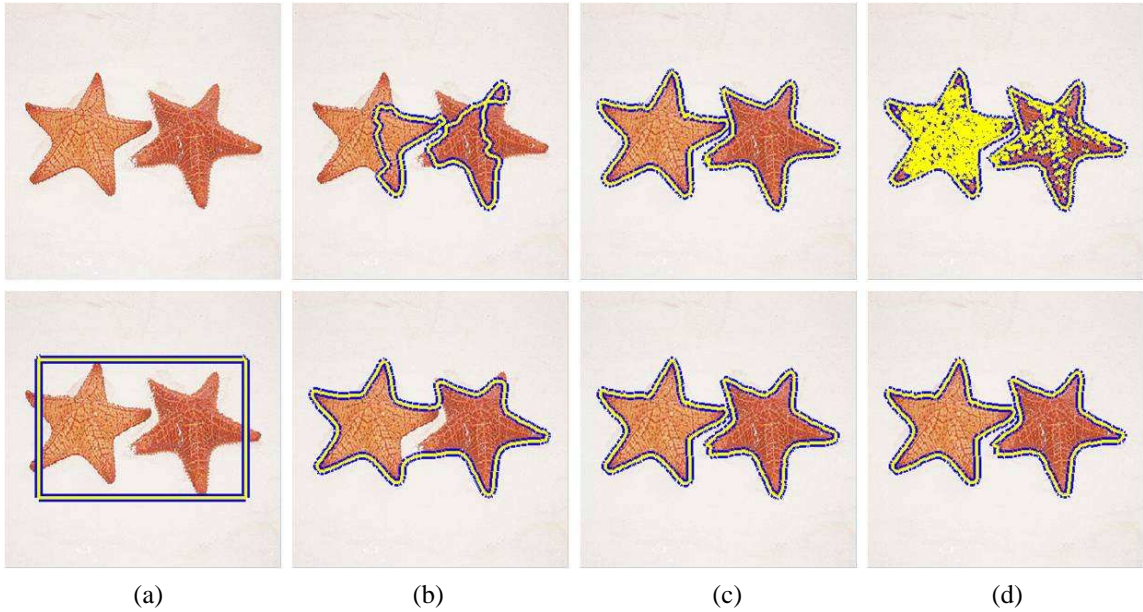


Figure 4.5: Performance of several active contour models for a starfish image.

Table 4.5: Computational cost of the starfish image.

Active Contours	Computational Time		
	Iterations	Time (s)	Average time (s)
GAC	240	422.11	1.76
ACWE	10	4.35	0.44
RSF	30	17.45	0.58
LRAC	1500	315.22	0.21
LRES	275	547.36	1.99
LREK	310	90.96	0.29

$c = 1$ for the GAC, $\sigma = 9$ for the RSF, $r = 30$ and F_{MS} for the LRAC, $l_{initial} = 30$, $\Delta l = 5$, and $\tau = 10$ for the LRES, $d_{initial} = 30$, $\Delta d = 5$, $\tau = 0.1$ and F_{MS} for our LREK.

In Figure 4.5, there are two separate starfishes. By setting $\omega = 1$, we let the GAC's contour to shrink since the initial contour is placed mostly outside the starfishes. However, after 240 iterations, it does not give a complete segmentation outcome. The RSF not only detect the starfishes but also the noisy pixels on the starfishes. With as much as 1500 iterations, the LRAC's contour is still unable to move into the concave part in between two starfishes thus give a connected starfishes as an segmentation result. The ACWE, LRES, and our LREK is capable to provide an actual boundary of the two separate starfishes. Because, the ACWE separate the image by calculating two piecewise constant of means intensity which in this case best approximate homogeneous foreground and background of the starfishes. With local adaptation process, the LRES and LREK does not have problems segmenting object with various concave shape. In spite of that, our LREK only consumes 90.96 seconds for 310 iterations which is faster than LRES with

Table 4.6: Computational cost of the bear cartoon image.

Active Contours	Computational Time		
	Iterations	Time (s)	Average time (s)
GAC	70	74.48	1.06
ACWE	10	7.79	0.78
RSF	40	33.34	0.83
LRAC	2000	385.07	0.19
LRES	190	404.92	2.13
LREK	240	59.92	0.25

547.36 seconds for 275 iterations.

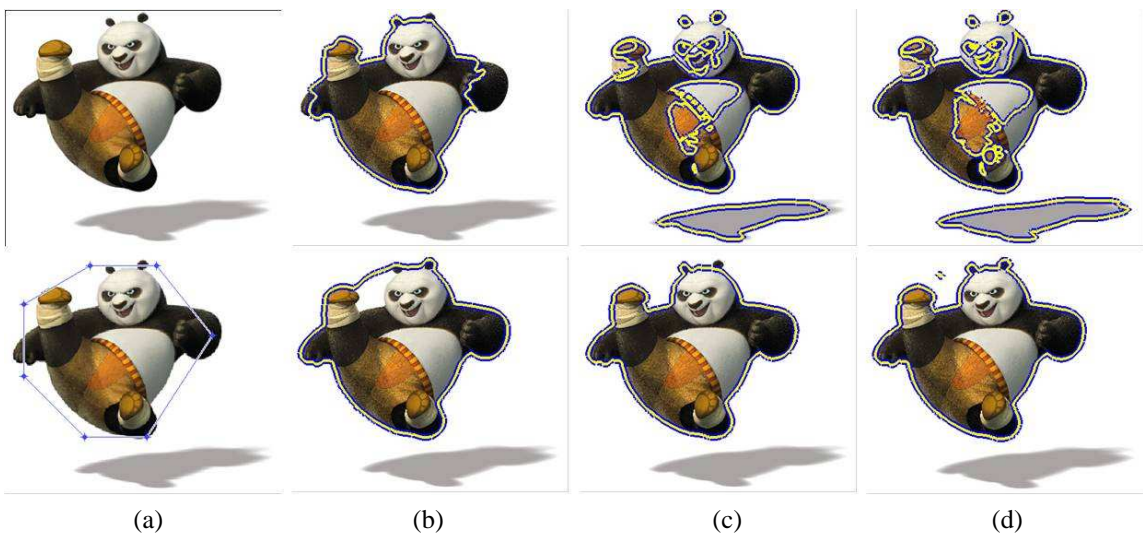


Figure 4.6: Performance of several active contour models for a bear cartoon image.

Figure 4.6 is a bear cartoon image with size 273×320 pixels. The following parameter are respectively set: the RSF with $\sigma = 19$, the LRAC with $r = 15$ and F_{MS} , the LRES with $l_{\text{initial}} = 30$, $\Delta l = 5$, and $\tau = 20$, the LREK with $d_{\text{initial}} = 15$, $\Delta d = 5$, $\tau = 20$, and F_{MS} .

An initial contour in Figure 4.6 is set manually by determining each point in the image and connecting that point to create a region of initial contour. So that, the user can interact to determine the initialization. This image contains two separate objects which are the bear cartoon and its shadow. However, the shadow is undesired as a segmentation outcome. The GAC generally can segment only the bear while ignoring the shadow. Although some part of the initial contour are inside the bear. We set $\omega = 3$ because the initial contour is mainly outside the object. High magnitude of balloon force helps the GAC to converge quickly with just 70 iterations. However, it constantly moves inward thus misclassifies some parts of an ear and two hands. The ACWE and RSF not only include the shadow as segmentation result but also divide the bear as several objects. This is due to the object contains various intensity region. Meanwhile the RSF

Table 4.7: Computational cost of the T-shape image.

Active Contours	Computational Time		
	Iterations	Time (s)	Average time (s)
GAC	55	17.33	0.32
ACWE	20	6.71	0.34
RSF	270	58.48	0.22
LRAC	1600	213.88	0.13
LRES	100	157.09	1.57
LREK	140	17.19	0.12

capture more details than the ACWE because it uses small kernel to be convolved to all image regions. With average computational time 0.78 and 0.83 second per iteration, they consume similar computational cost per iteration. However, the RSF requires 40 iterations more than required by ACWE to converge with only 10 iterations. Although, the iteration numbers for the LRAC is set to 2000, the contour is unable to move into concave part between head and foot. It is not easy to determine the optimal ball radius particularly when the object has various concave part. The LRES generally segments the bear although it misclassifies the ear part. This is perhaps due to small thin search line that might not reliably sample the pixels intensity thus confused and direct the contour wrongly. Also, the LRES is considered more time consuming where it requires 2.13 seconds per iteration compared to our proposed scheme which only consumes 0.25 second per iteration. Meanwhile, our LREK extracts complete object boundaries.

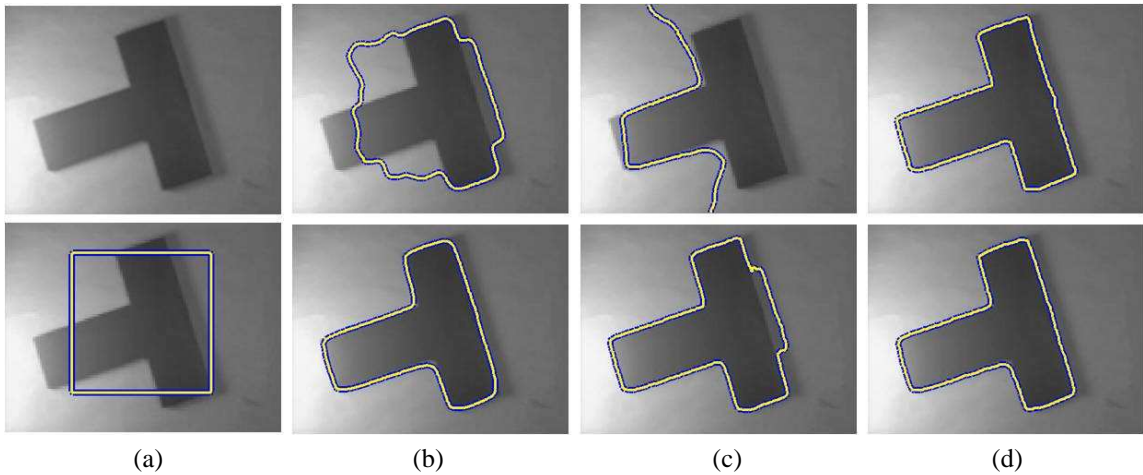


Figure 4.7: Performance of several active contour models for a T-shape image.

A T-shape object with non-uniform intensity in Figure 4.7 has 96×127 pixels of image size. The RSF's kernel is set with $\sigma = 3$, the LRAC's ball radius is set with $r = 10$ and F_{MS} , the length of LRES's search line is set to $l_{initial} = 10$, $\Delta l = 3$, and $\tau = 30$, and parameter for our LREK is set with $d_{initial} = 10$, $\Delta d = 5$, $\tau = 30$, and F_{MS} .

The T-shape object in Figure 4.7 has spatial variation of intensity inhomogeneity. With $\omega = 0$, the GAC has low speed and small range of capture, the GAC's contour is confused thus does not move capturing the object. The ACWE is confused with the non-uniform textures and tends to separate the image into brighter and darker areas. The RSF, LRAC, LRES, and LREK generally can deal with intensity inhomogeneity of the image. The RSF's final contour is correctly placed on the object. However, it consumes 270 iterations and 58.48 seconds to successfully place its contour on the object. To arrive at the object boundary, the LRAC's contour needs 1600 iterations and 213.88 seconds. Meanwhile, it ignores small intensity details in some corners of the T-shape object. The LRES just have a small problem with the shadow. It is confused with the shadow part and consider it as part of the object. Finally, by consuming just 140 iterations and 17.19 seconds, the T-shape can be segmented accurately without any problem by our scheme.

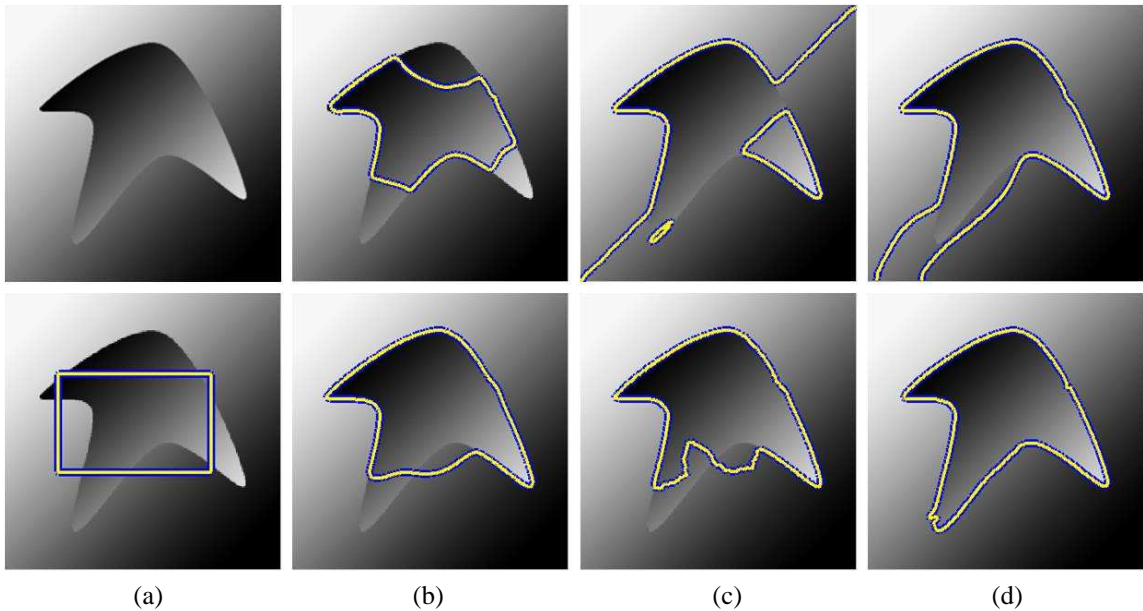


Figure 4.8: Performance of several active contour models for a synthetic heterogeneous textures image.

An object with heterogeneous texture without adding noise in Figure 4.8 has 200×200 pixels of image size. The parameters are given as follows: the RSF with $\sigma = 11$, the LRAC with $r = 40$ and F_{CV} , the LRES with $l_{\text{initial}} = 40$, $\Delta l = 5$, and $\tau = 10$, and our LREK with $d_{\text{initial}} = 10$, $\Delta d = 5$, $\tau = 50$, and F_{MS} .

The image in Figure 4.8 has heterogeneous textures where either its object or its background contains both brighter and darker intensities. It also contains various concave parts. Due to local consideration of image gradient, the GAC does not confuse with the overlapped intensity between the foreground and background. However, after its contour evolves for 500 iterations, the choice of $\omega = 0$ is unable to attract the contour to some corners of the object. By setting ω to be positive or negative, it just makes the contour shrink or expand with a constant speed while the

Table 4.8: Computational cost of the heterogeneous textures image.

Active Contours	Computational Time		
	Iterations	Time (s)	Average time (s)
GAC	500	718.41	1.44
ACWE	10	3.99	0.40
RSF	500	160.43	0.32
LRAC	550	133.64	0.24
LRES	300	658.35	2.19
LREK	350	68.91	0.19

contour actually needs to shrink and expand accordingly. The piecewise-constant approximation of global means intensity leads to image separation according to the image area that represented by its intensity. Thus, the brighter area is considered as the foreground while the darker area as the background. We observed that the RSF, LRAC, and LRES segment most of the object parts except the part where the intensities of foreground and background are hardly distinguished. They successfully segment the part where the difference between foreground and background can be clearly distinguished. All these region-based methods with local constraint do not confuse the overlapped intensities between the foreground and the background due to its local consideration. Their total computational time are 160.43, 133.64, and 658.35 seconds for the RSF, LRAC, and LRES, respectively. On the other hand, our scheme provides a complete segmentation result. It consumes 68.91 seconds for 350 iterations with average computation time 0.19 second per iteration.

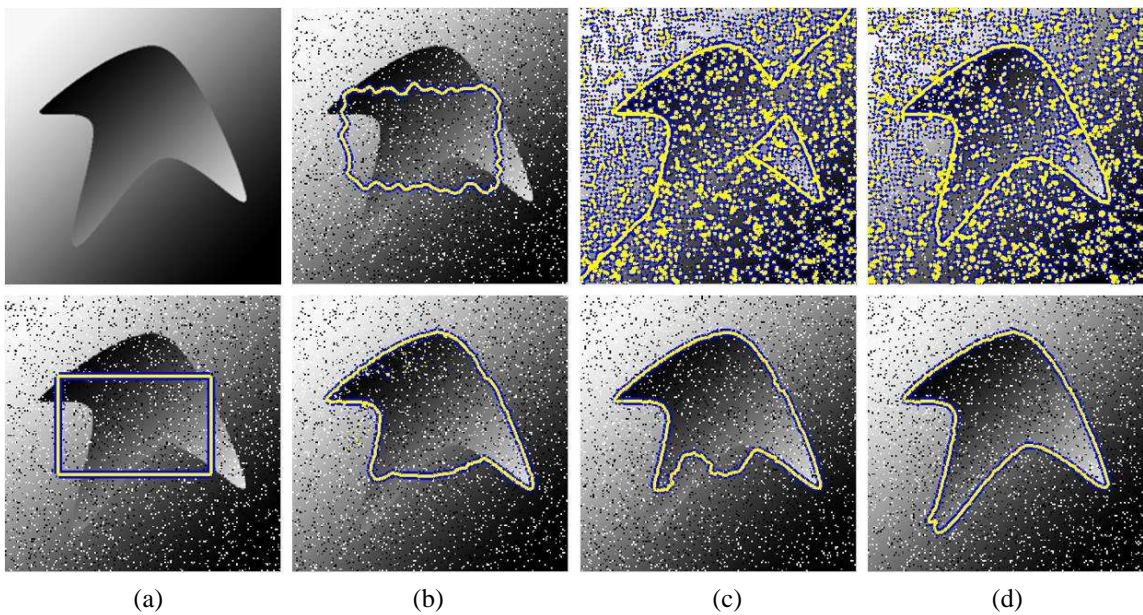


Figure 4.9: Performance of several active contour models for a synthetic heterogeneous texture image with added salt and pepper noise.

Table 4.9: Computational cost of the heterogeneous textures image with salt and pepper noise.

Active Contours	Computational Time		
	Iterations	Time (s)	Average time (s)
GAC	220	308.20	1.40
ACWE	10	21.48	2.15
RSF	30	53.85	1.80
LRAC	550	280.65	0.51
LRES	300	626.59	2.09
LREK	400	111.34	0.28

A noisy heterogeneous textures image in Figure 4.9 has size 200×200 pixels. The following parameters are used: $\sigma = 13$ for the RSF, $r = 50$ and F_{CV} for the LRAC, the LRES with $l_{\text{initial}} = 40$, $\Delta l = 5$, and $\tau = 10$, and our LREK with $d_{\text{initial}} = 15$, $\Delta d = 5$, $\tau = 45$, F_{MS} .

Figure 4.9 contains the same image in Figure 4.9 with added salt and pepper noise. Since the GAC uses edge information of image gradient, it is sensitive to noise. Even though the GAC's contour move for 220 iterations it does not move anywhere because it is stuck by the gradient pixels of the salt and pepper noise. Although the ACWE requires only 10 iterations with 21.48 seconds it still separate the image into brighter area as the object and the darker area as the background. Also, it includes white and black pixels of the noise as the object. With only 30 iterations, the RSF almost captures the whole object. However, it also includes the noise as part of the object. Even though it uses local window, this is perhaps due to convolution of two fitting functions of the kernels to all over the image. It is different to the rest of the three methods: the LRAC, LRES and LREK. They use local image intensity and compute it using local window spread on the contour. Even so, the LRAC and LRES cannot segment effectively the lower part of the object where the intensities of the foreground and background are less distinguishable. Nonetheless, our method still provides successful segmentation result even in the presence of noise with average computational time 0.28 second per iteration.

An ultrasound image of size 221×217 is shown in Figure 4.10. The following parameter are used: the RSF with $\sigma = 21$, the LRAC with $r = 15$ and F_{MS} , the LRES with $l_{\text{initial}} = 15$, $\Delta l = 5$, and $\tau = 20$, and our LREK with $d_{\text{initial}} = 15$, $\Delta d = 5$, $\tau = 10$, and F_{MS} .

Since the initial contour is placed entirely inside the object, the balloon force is set to -1 to constantly grow the contour capturing the object. Noisy environment, however, makes it stuck thus it is unable to further capture the actual object. The ACWE and RSF consider all the white pixels as the object. While the RSF is capable in handling intensity inhomogeneity, the ACWE cannot distinguish that kind of spatial variation. Consideration of local image intensity makes the

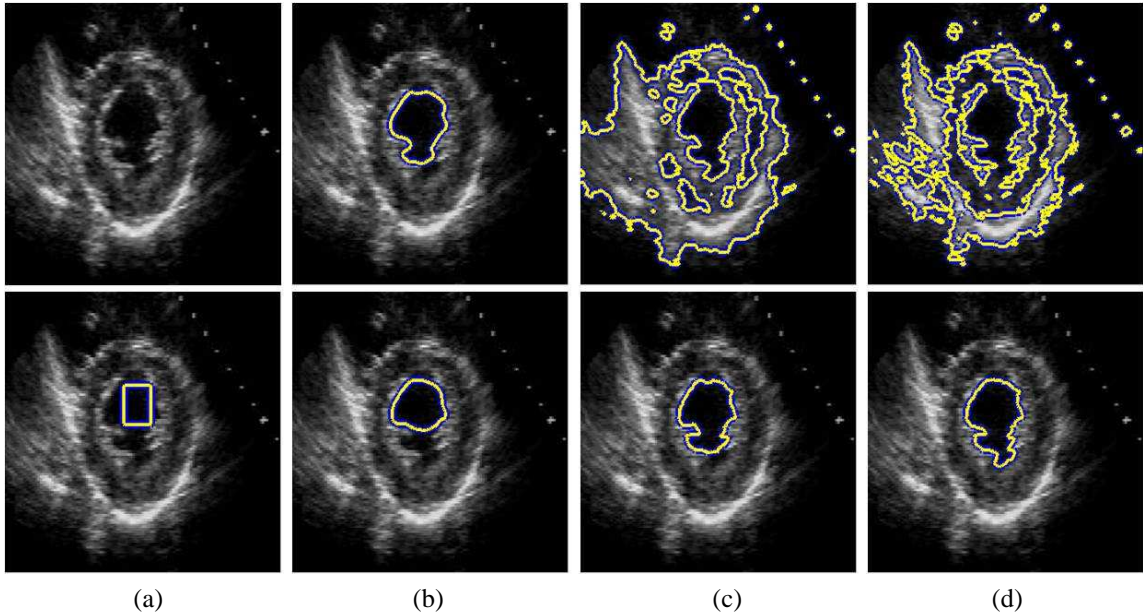


Figure 4.10: Performance of several active contour models for an ultrasound image.

Table 4.10: Computational cost of the ultrasound image.

Active Contours	Computational Time		
	Iterations	Time (s)	Average time (s)
GAC	150	80.37	1.53
ACWE	10	5.11	0.511
RSF	35	25.36	0.72
LRAC	300	29.99	0.10
LRES	150	98.49	0.66
LREK	240	29.90	0.12

Table 4.11: Computational cost of the corpus callosum image.

Active Contours	Computational Time		
	Iterations	Time (s)	Average time (s)
GAC	180	549.79	3.05
ACWE	10	41.67	4.17
RSF	25	186.72	7.47
LRAC	2500	689.17	0.28
LRES	670	923.96	1.38
LREK	1000	305.06	0.31

LRAC, LRES, and LREK act similar to the GAC rather than the ACWE and RSF. Even though the iteration numbers is set as much as 300, problem of limited capture range makes the LRAC's contour unable to evolve further into the lower part of the object. With extendable search line, the LRES does not have problem of limited capture range. It is just confused with the small area in the lower part where its intensity is less distinguishable. On the other hand, with an ability of expandable kernel, our scheme provides more complete segmentation outcome although its kernel scale is set to 15 pixels similar to the LRAC.

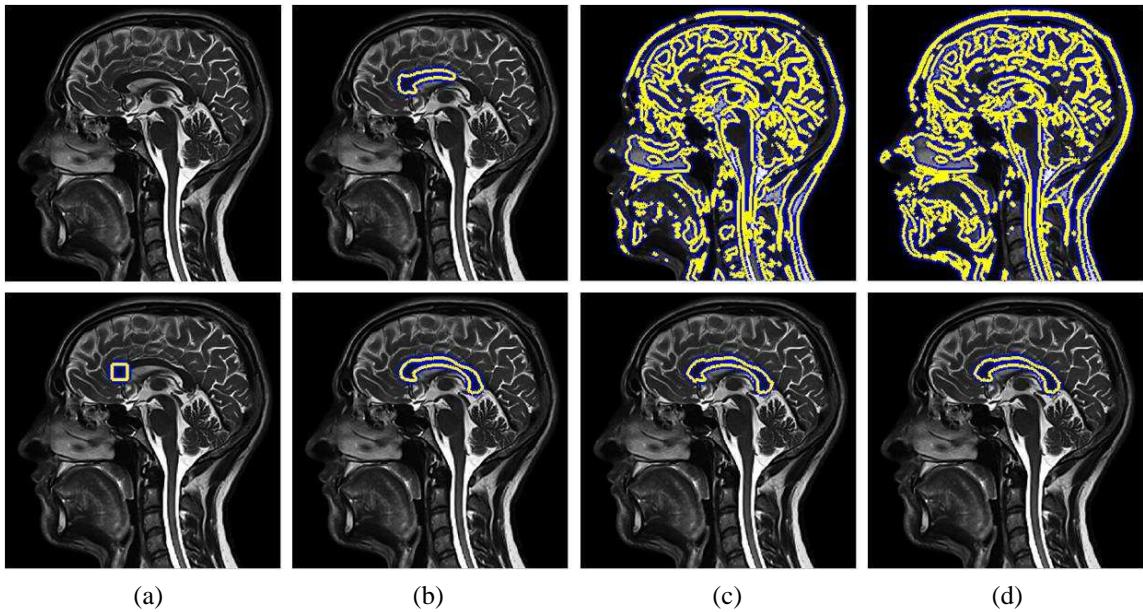


Figure 4.11: Performance of several active contour models for a corpus callosum of an MR brain image.

A magnetic resonance image (MRI) of a corpus callosum part of a brain in Figure 4.11 is of size 550×550 . For each scheme the parameter are respectively set as follows: the RSF with $\sigma = 41$, the LRAC with $r = 20$ and F_{CV} , the LRES with $l_{\text{initial}} = 20$, $\Delta l = 3$, and $\tau = 10$, and our LREK with $d_{\text{initial}} = 15$, $\Delta d = 5$, $\tau = 20$, and F_{MS} .

For the corpus callosum image in Figure 4.11, the initial contour is placed to the right of

the corpus callosum. The constant motion ω is set to -1.5 so the contour move outward from initial contour that is totally inside the object. However, it is stuck in the middle of the corpus callosum. The ACWE and RSF tend to segment the whole part of the image instead of the corpus callosum. The contours of LRAC, LRES and LREK are able to move into the concave part. It is worth to note that by setting the LRAC's ball radius to 15 pixels similar with our LREK's kernel scale, the LRAC's contour is stuck. To have larger capture range, its radius is set to 20 pixels. The adaptive statistics of expandable kernel gives the advantages of expandable capture ranges so that with just 15 pixels our model is able to trace a complete corpus callosum without getting stuck. Moreover, it requires less iteration number with 1000 iterations than the LRAC which requires 2500 iterations. It converges faster with only 305.06 seconds than computational time of 923.96 seconds required by the LRES.

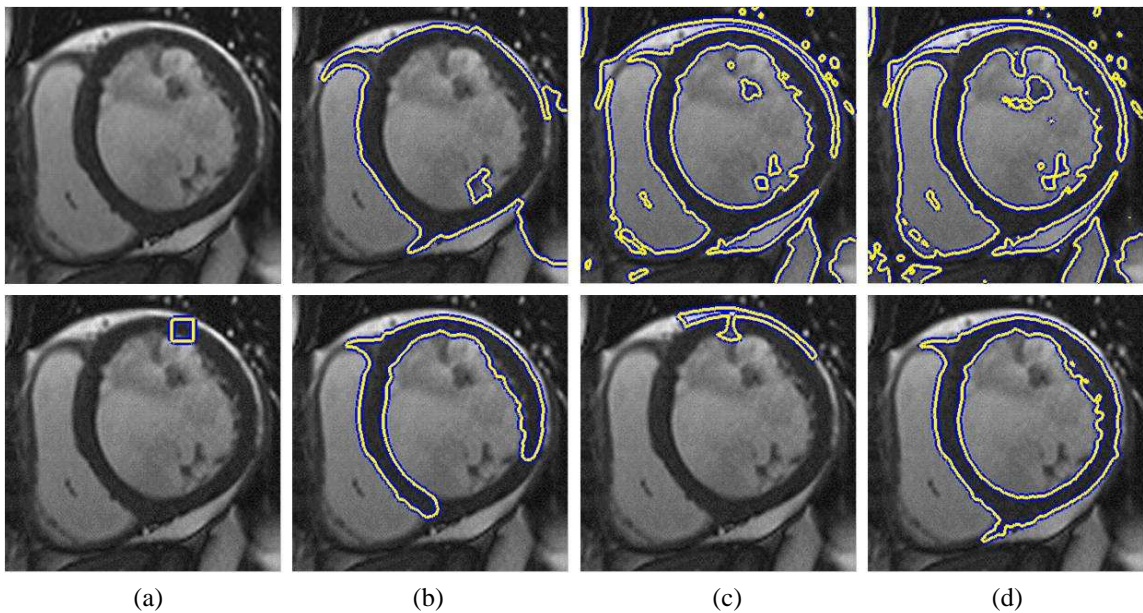


Figure 4.12: Performance of several active contour models for a left ventricle of cardiac MR image.

Figure 4.12 contains left ventricle of cardiac MRI (CMRI) with size 324×324 . Parameter settings used are as given: the RSF with $\sigma = 17$, the LRAC with $r = 25$ and F_{MS} , the LRES with $l_{\text{initial}} = 30$, $\Delta l = 5$, and $\tau = 20$, our LREK with $d_{\text{initial}} = 30$, $\Delta d = 5$, $\tau = 20$, and F_{MS} .

Left ventricular segmentation requires segmentation of epicardial and endocardium boundary simultaneously and as a result it will form a ring-like object. Initial contour is placed inside the ring-like object. With $\omega = -1$, the GAC is able to trace most of the epicardial boundary however it has boundary leakage problem in the weak boundary. When segmenting endocardium, it moves ignoring the endocardium particularly in some blur and weak boundaries and as a result only a small amount of pixels is left. The ACWE and RSF capture all brighter intensity regions as the object. The RSF, on the other hand, captures more intensity details and handle non-uniform

Table 4.12: Computational cost of the ventricle image.

Active Contours	Computational Time		
	Iterations	Time (s)	Average time (s)
GAC	900	2047.82	2.28
ACWE	10	9.01	0.90
RSF	30	25.89	0.86
LRAC	4000	1071.63	0.26
LRES	750	2208.45	2.94
LREK	1700	724.93	0.42

textures while the ACWE ignores some details and its spatial intensity variation. Before radius of the LRAC's ball is set to 25, $r = 30$ is used. However, the LRAC's contour shrink and disappear immediately. With $r = 25$, it evolves capturing the ring-like object. However, after it reaches 3000 iterations the contour stops at two intersections. By adding number of iterations to 4000, it is no longer evolve. This is perhaps due to the distance between the contour as the center of fixed-radius ball and the boundary may be too far from the radius. Hence, the LRAC's ball is unable to include appropriate statistics as a force to drive the contour to the real boundary. As a result, it reaches local minima and stops even though we let it moves for 1000 iterations more. The LRES seems confused which direction to guide the contour. Instead of tracing the ring-like object, it just evolves in the epicardial boundary. Nevertheless, our proposed scheme has enough capture range to detect both epicardial and endocardium simultaneously. It has no problem to trace concave shape object of the ring-like object. In addition, our LREK requires 1700 iterations and 2208.45 seconds to arrive at the intended boundary.

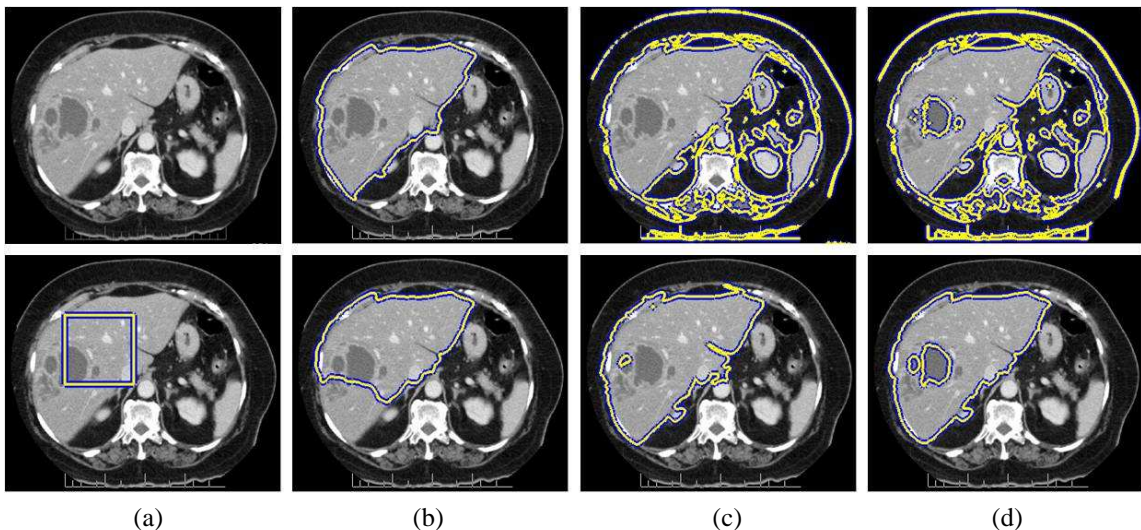


Figure 4.13: Performance of several active contour models for a liver tumor of a CT scan image.

Figure 4.13 is a liver tumor of a computed tomography (CT) scan image with size 315×368 pixels. The parameters used for this image are as follows: the RSF with $\sigma = 23$, the LRAC with

Table 4.13: Computational cost of the liver tumor image.

Active Contours	Computational Time		
	Iterations	Time (s)	Average time (s)
GAC	250	492.23	1.96
ACWE	10	11.67	1.17
RSF	30	41.71	0.31
LRAC	4000	1014.72	0.25
LRES	620	2514.90	4.06
LREK	1350	580.55	0.43

$r = 29$ and F_{MS} , the LRES with $l_{initial} = 40$, $\Delta l = 5$, and $\tau = 15$, our LREK with $d_{initial} = 29$, $\Delta d = 5$, $\tau = 10$, and F_{MS} .

In Figure 4.13, liver region as well as several tumor areas are desirable as segmentation outcome. By setting $\omega = -3$ and initial contour totally inside the object, high speed of the balloon force does not make the GAC's contour stuck. Hence, it is able to evolve capturing the liver region although it does not include the tumor and misclassifies some small liver region. Again, these two global regional models tend to segment all image region with more organs while the liver and tumors are the only intended segmentation object. While the ACWE includes less object details of the image, the RSF captures more details such as the tumors. Perhaps this is as an advantage of convolving small kernel into all image area. The LRAC's contour gets stuck by the tumors thus cannot move into lower part of the liver region. The LRES traces all the liver region and half of small tumor area but still has some spill-over area on the liver boundary. Its average computational time reaches 4.06 seconds for each iteration where its total computational time costs 2514.90 seconds. Nonetheless, our LREK's contour evolves with a large capture range from its initial contour until reaching the boundary of the liver region while excluding some tumor regions. It demonstrates an ability of our LREK in splitting and merging in order to detect liver boundary and two tumors simultaneously where this is as the advantage of level set formulation in handling topological changes. In addition, our LREK is more effective and efficient in segmenting the image which requires less iteration number than the LRAC and takes less computational time compared to the LRES while gives more complete segmentation result.

An X-ray hand image in Figure 4.14 has size 255×180 . Following parameter are used: the RSF with $\sigma = 17$, the LRAC with $r = 15$ and F_{CV} , the LRES with $l_{initial} = 40$, $\Delta l = 5$, and $\tau = 15$, the LREK with $d_{initial} = 15$, $\Delta d = 5$, $\tau = 10$, and F_{CV} .

Figure 4.14 depicts performance of each model in segmenting the bone of X-ray image. Placement of initial contour both inside and outside the object makes the GAC's contour stuck in

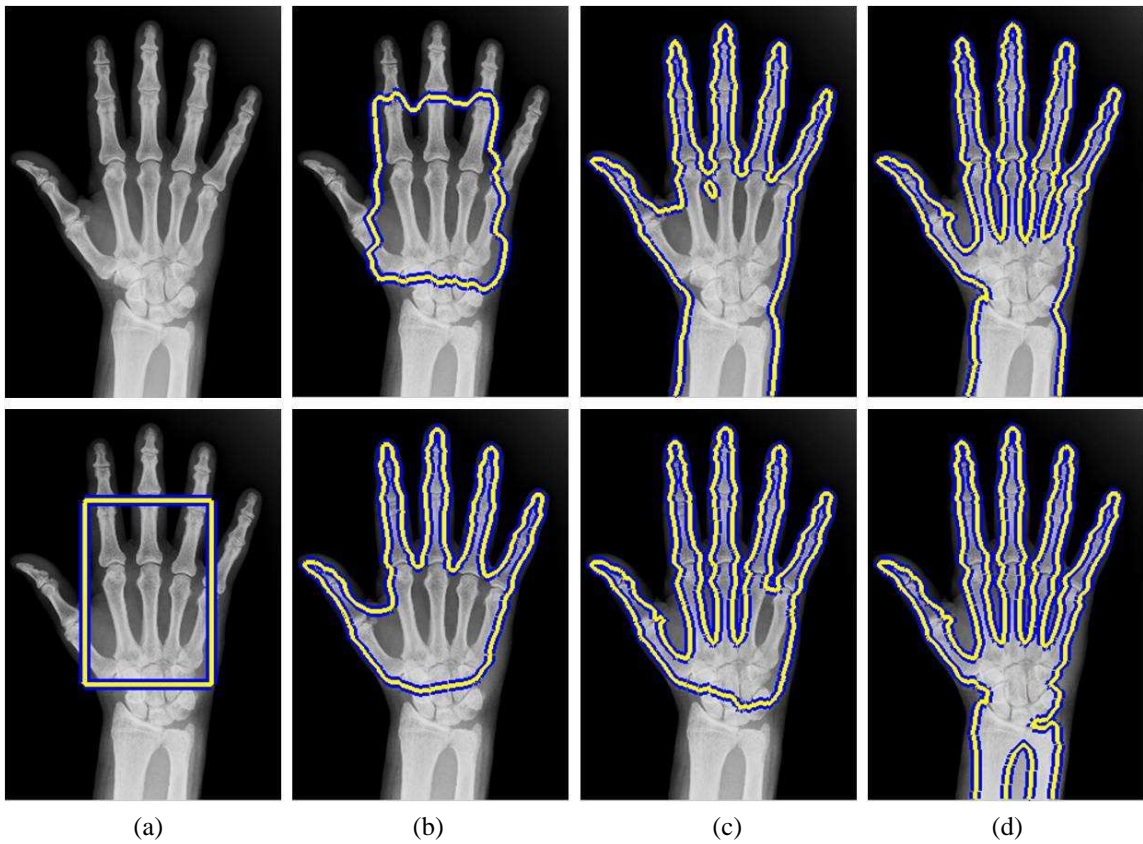


Figure 4.14: Performance of several active contour models for a bone part of an X-ray hand image.

Table 4.14: Computational cost of the bone image.

Active Contours	Computational Time		
	Iterations	Time (s)	Average time (s)
GAC	100	74.30	0.74
ACWE	10	4.39	0.44
RSF	100	45.76	0.45
LRAC	660	112.35	0.17
LRES	300	658.35	2.19
LREK	660	188.59	0.29

the wrong image gradient. Hence, it cannot evolve and arrive at the actual boundary. The ACWE and RSF almost traces whole bone part but the ACWE includes more of the skin region than the RSF. The LRAC's contour cannot move into finger area which is considered as the concave shape and lower part of the hand perhaps due to its limited capture range. The LRES, which is able to handle concave part, can move into some fingers area. However, local statistics on the search line may not enough to describe the local image intensity. This lack of information, hence, makes the search line does not produce any force to pull the contour towards real boundary. It is confused then unable to move into the lower part of the hand. Meanwhile, our method provides segmentation of the whole bone and completely excludes the skin part. It has a large capture range to reach concave boundary of the fingers and lower part of the hand. We also notice that LREK's contour is able to split excluding the skin part on the lower part of the hand.

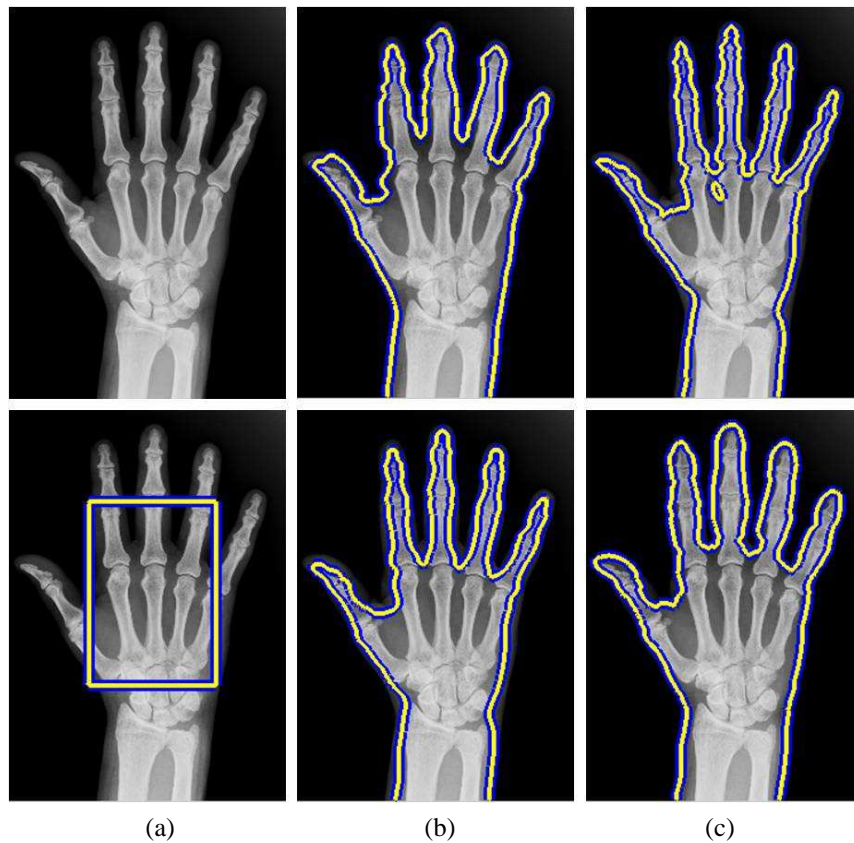


Figure 4.15: Performance of several active contour models for a skin part of an X-ray hand image.

Figure 4.15 contains the same image in Figure 4.14 with size 255×180 pixels. In the first row, there are original image, segmentation result of the GAC and RSF, respectively. The initial, final contour for the LRAC and LREK are respectively plotted in the second row. The following parameter are used for each model: the GAC with $\omega = 3$, the RSF with $\sigma = 101$, the LRAC with $r = 100$ and F_{CV} , our LREK with $d_{\text{initial}} = 100$, $\Delta d = 5$, $\tau = 10$, and F_{CV} .

In Figure 4.15, we show segmentation outcomes on the skin part instead of the bone. Es-

Table 4.15: Computational cost of the skin image.

Active Contours	Computational Time		
	Iterations	Time (s)	Average time (s)
GAC	125	180.02	1.44
RSF	20	48.94	2.45
LRAC	330	351.11	1.06
LREK	450	64517.94	143.37

pecially for the GAC, we put the initial contour entirely outside of the object and use high speed balloon force with $\omega = 3$. The GAC detects most of the skin part while in the weak edges it passes over the actual boundary. Even though we set large value for the sigma of the RSF's Gaussian kernel and radius of the LRAC's ball, their results are approximately the same with the ACWE in Figure 4.14. In our formulation, we can show the role of the Gaussian function to segment the blur or smooth boundary. By setting large value of sigma, our Gaussian LREK provides most of the skin part. It is worth to note that in the RSF we could not find the smoothness effect of the Gaussian property in both choice of small or large scale of the kernel. In addition, the RSF obtains accurate segmentation outcome with small scale sigma. With sufficiently large scale, it is insensitive to the initial condition similar to the global region-based model. However, it acts like the global region-based model and ignores some object details to be captured.

In summary, all these experiments verify that our LREK provides more desirable and efficient segmentation outcomes. Scalable local regional information enables our method to quickly converge into desired objects with noises, non-uniform, and heterogeneous textures. Adaptive local statistics of expandable kernel allows our LREK to reach any deep concavity with a large capture range. Our Gaussian LREK has an ability to segment the smooth or blur boundary. Level set formulation makes our LREK topologically flexible.

4.2 Directional LREK (DLREK)

In this section, we test performance of the DLREK on real scene of medical images. They are two MR images of brain tumor, cardiac MR image of left ventricle of the heart, and ultrasound image. The original image is shown in the first column of each tested image. The initial contour and the final contour on the positive-edge object and the negative-edge object are plotted on the second, third, and fourth column of each tested images in Figures 4.16-4.19, respectively. All of the tested images contain two objects of different edge's types. They are the positive-edge object which are considered as a darker object lies on a brighter background and the negative one as a brighter object on a darker background.

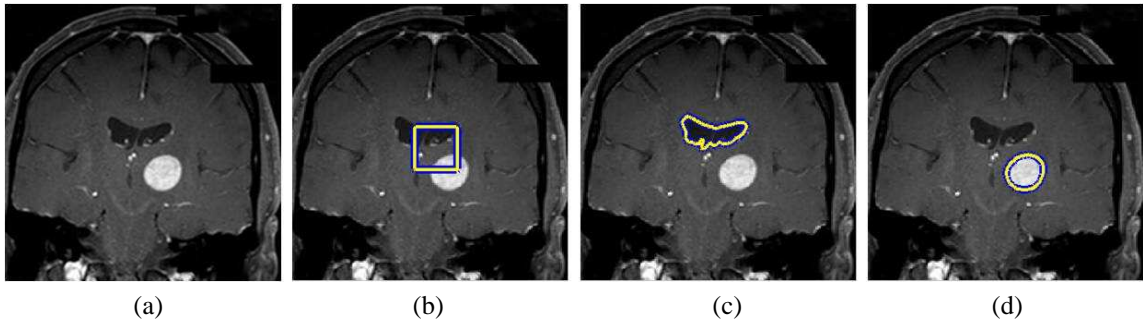


Figure 4.16: Performance of our DLREK for an MR brain tumor image

The image in Figure 4.16 has two objects of interest to be captured. They are a lateral ventricle as the positive-edge object and a bright spot of a tumor as the negative-edge object. We see that our model segments two desirable objects accurately. The contour evolves then finally converges in both objects using the same initial contour position. By setting $\beta = +1$, the lateral ventricle as the positive-edge object can be correctly segmented as in Figure 4.16 2(c). On the other hand, we just set $\beta = -1$ to obtain an accurate segmentation outcome of the bright spot of the tumor (see column d).

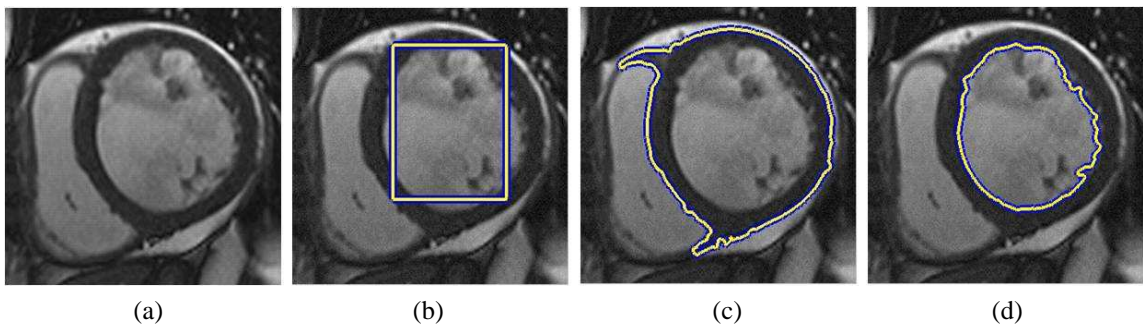


Figure 4.17: Performance of our DLREK for a CMR left ventricle image

Figure 4.17 contains the same image in Figure 4.12. There are two candidates of left ventricular segmentation which consist of epicardial boundary as positive-edge object and endocardial boundary as negative-edge object. By setting $\beta = +1$ and $\beta = -1$, positive-edge of epicardial boundary and negative-edge of endocardium boundary are respectively segmented by our DLREK. As a special help to drive the contour away from undesired local image intensity, ω is chosen to be -1 so that the local balloon force gives outward direction to capture epicardial boundary in Figure 4.17 (c) and $\omega = +1$ is to allow the contour locally shrink in the undesired image area. After it has reached the intended object, the force will be switched back to the SLR force.

Figure 4.10 contains an ultrasound image of a small baby. In this image, we want to capture the positive-edge object while ignoring small baby which is the negative-edge object and vice

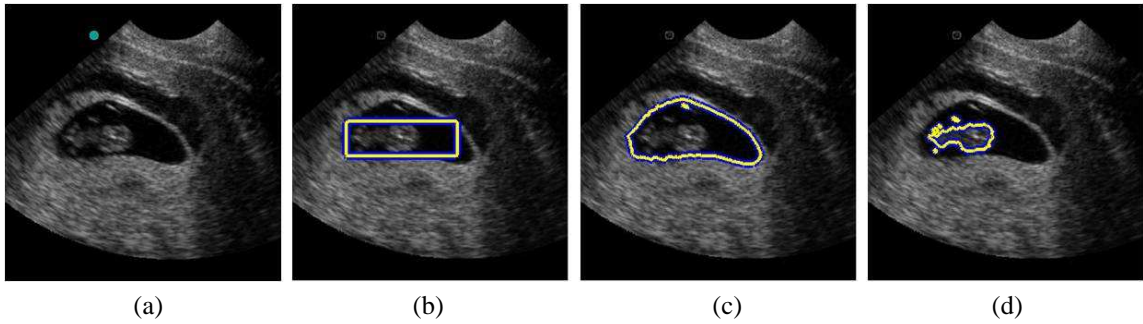


Figure 4.18: Performance of our DLREK for an ultrasound image of a small baby

versa. To detect positive-edge object, β and ω are set to be $+1$ and -1 , respectively. Since the initial contour is put inside the positive-edge object, $\omega = -1$ is a special help to grow the contour detecting the object. Once the contour is near the desirable boundary, the force is switched back to the SLR force. Otherwise, the balloon force will make the contour further grow ignoring the boundary. Next, the parameters are chosen to be $\beta = -1$ and $\omega = +1$. $\omega = +1$ is selected so that it gives an inward direction for balloon force to capture the small baby as the negative-edge object.

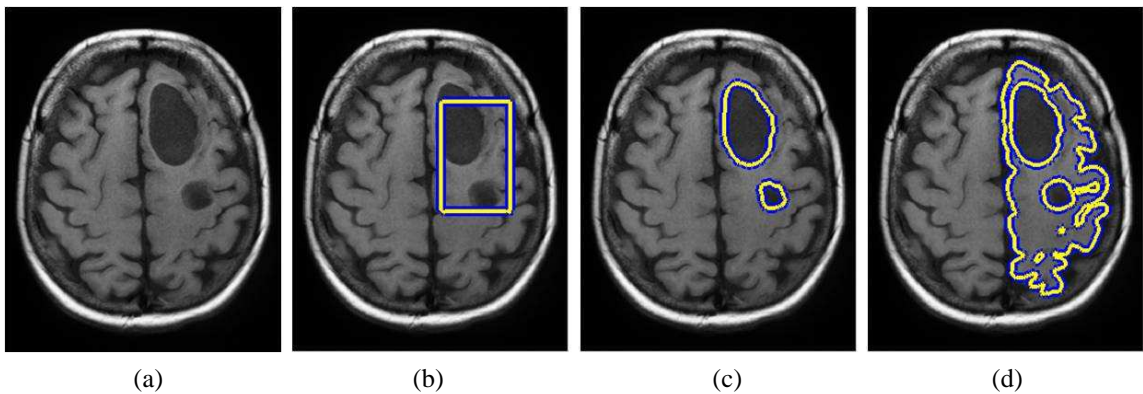


Figure 4.19: Performance of our DLREK for an MR brain tumor image

In Figure 4.19, there are two segmentation candidates that are two spots of tumors and the right part of the brain. The tumors are considered as two separate positive-edge objects. The right part of the brain that has two separate tumors is considered as the negative-edge object. A contour tries to segment the tumors only and the brain without the tumors. As the advantage of level set formulation, an initial contour may split capturing two separate tumors accurately as two positive-edge objects (see column c). The fourth column of Figure 4.19(d) demonstrates an ability of our DLREK in splitting and merging to detect the right part of the brain but exclude the tumors instead. The right part of the brain can be captured conveniently without any leaking into the tumors or the left part of the brain. Our model has a large capturing area to evolve from its initial contour until finally reach concave shape of the boundary of the brain.

In addition, all these experiments validate that the DLREK is capable in tracing two edge's type objects conveniently without getting stuck by any noisy pixels. The scalable kernel samples intensity statistics with an appropriate scale thus deemphasizes role of small noisy pixels by taking averages of intensity profiles within the kernel.

CHAPTER V

CONCLUSION

5.1 Thesis Summary

A new active contour model called the LREK that utilizes local region-scalable statistics on expandable kernels has been presented in this thesis. The scalable local regional information is intensity profile of the pixels on a set of expandable kernels that centered and distributed at the contour. Each kernel is designed to be of adaptive scale so that it can navigate the contour front toward the object boundary with expandable capture range. The intensity statistics on a set of kernels are utilized to produce local region-scalable force, enabling the contour to segment image with intensity inhomogeneities and heterogeneous textures. We compare our LREK over other active contour schemes. Our scheme is less sensitive to noise and initial condition than the edge-based models. When compared to such global models, our method is more robust to noise than the ACWE and RSF. Although the RSF model uses Gaussian kernel, we cannot find the effect of Gaussian function in small or large sigma value. On the other hand, our Gaussian LREK is capable in tracing the smooth boundary, hence, showing the role of Gaussian function in the segmented image. From the experiments, the advantages of our method over the LRAC is an ability to reach concave shape with a large range of capture. Furthermore, when compared to local region-based active contour that uses extendable search line such as the LRES, our method provides more effective and efficient segmentation results. The long thin LRES's search line may not reliably sample the local intensity, hence, confused and unable to attract the contour to the true boundary. Moreover, unscalable search line makes the LRES being computationally expensive. On the other hand, we found that our model converges to the intended boundary quickly. In addition, to choose objects of desirable edge's type, we also present a directional local region-scalable active contour using expandable kernel (DLREK). While magnitude of intensity difference is used in local adaptation statistics in order to detect object's boundary, sign of the difference is utilized to automatically switch appropriate force depending on local image edge's type. With directional property, one initial contour placement results in two segmentation outcomes of desirable edge's type. Hence, not only is our model capable in handling images with noises, non-uniform, and heterogeneous textures with quick convergence, it also has a large capture range to trace concave shape object. In addition, formulation of our method in the level set enables our active contour to naturally split and merge.

5.2 Discussion

5.2.1 Global versus Local Models

Such global models have one energy function that trying to segment the object by approaching whole image intensity with its statistical properties. That is different to the local model where each of the energy function is defined on many local area distributed on the contour. The energy function of global models should have one global minima while each of the energy function of the local models should have one local minima.

5.2.2 Effect of Localization to Initialization

The global region descriptor may have more flexibility in initialization than the one with local constraint. This flexible initialization, however, may not have choices to get different object of segmentation candidate by placing different initial condition. Wherever initial contour is put, it will produce similar segmentation outcome. In fact, several images may have complex appearance where exist several objects. From several objects, a particular object may be desirable as segmentation outcome. Such global models have tendency to detect all object no matter where initial condition is put. It may not be able to choose particular object of interest from several object existing on the image. Localization property of the proposed method, on the other hand, can be a desirable property. As a result of the localization, this desirable property, even though requires clever initialization, is able not only to separate objects from its background but also from undesired other objects according to initial contour placement.

5.2.3 Relation between Active Contour Models

Unlike the local region-scalable models, the local region-based models are unable to change the scale of the local region. These models just consider a local intensity region and ignore the rest of image features, hence, with extremely small scale kernel they have close relation with the edge based or local region-based models which considers only a small edge pixels.

We also see that global region-scalable models has close relation to the global region-based models where the scalable region of the kernel has a degree of freedom to choose its scale to be small to approaches local intensity details or to be large to meet behaviour of global region-based models. On the other hand, the local region-scalable models illustrate the connection of the relation between the edge-based or local region-based models and global region-based models. One could see that behaviour of the LRAC is controlled by the fixed-radius ball while the width of the edge pixels of the edge-based models are controlled by sigma parameter of the edge indicator

where mostly σ is chosen to be 1. Considering the ball radius is either 1 or ∞ , with the radius of 1 then it acts similar to the edge-based or the local region-based models while with the radius of ∞ the ball will include all intensity statistics all over the image, hence, acts similar to the global region-based models.

Hence, in our proposed model we let the relation between edge and region-based models acts in the evolution process automatically. The kernel expands itself from its initial scale to the optimum scale according to the local image feature so that the kernel finds its optimum scale to detect the boundaries. In our formulation, from extremely small initial scale of the kernel, i.e., $d = 1$, the adaptive local statistics can reach the maximum scale as large as possible ($d = \infty$) which covers all image intensity. With $d = 1$, our formulation of DLREK with additional balloon force is similar to the GAC with additional balloon force too. The GAC considers only small pixels of image gradient where the width is determined by σ parameter of Gaussian function. With $d = 1$, such small kernel only considers intensities for 1 pixel similar to the GAC. Additional balloon force can be a special help to expand capture range of such small kernel while switching parameter will help to switch it back to SLR force once it arrives at the boundaries.

References

- [1] Kass, M., Witkin, A., and Terzopolous, D. Snakes: Active contour models. International Journal of Computer Vision 1, 4 (1988): 321-331.
- [2] Osher, S., and Sethian, J. Front propagating with curvature-dependent speed: Algorithms based on Hamilton-Jacobi formulations. Journal of Computational Physics 79, 1 (1988): 12-49.
- [3] Caselles, V., Kimmel, R., and Sapiro, G. Geodesic active contours. International Journal of Computer Vision 22, 1 (1997): 61-79.
- [4] Caselles, V., Catta, F., Coll, T., and Dibos, F. A geometric model for active contours. Numerische Mathematik 66, 1 (1993): 1-31.
- [5] Malladi, R., Sethian, J. A., and Vemuri, B. C. Shape modelling with front propagation: A level set approach. IEEE Transaction on Pattern Analysis and Machine Intelligence 17, 2 (1995): 158-175.
- [6] Cohen, L. D., and Cohen, I. Finite element methods for active contour models and balloons for 2-D and 3-D images. IEEE Transaction on Pattern Analysis and Machine Intelligence 15, 11 (1993): 1131-1147.
- [7] Xu, C., and Prince, J. L. Snakes, shapes, and gradient vector flow. IEEE Transaction on Image Processing 16, 8 (1998): 359-369.
- [8] Li, B., and Acton, S. T. Active contour external force using vector field convolution for image segmentation. IEEE Transaction on Image Processing 16, 8 (2007): 2096-2106.
- [9] Wang, T., Cheng, I., and Basu, A. Fluid vector flow and applications in brain tumor segmentation. IEEE Transaction on Biomedical Engineering 56, 3 (2009): 781-789.
- [10] Zimmer, C., and Olivo-Marin, J.-C. Coupled parametric active contours. IEEE Transaction on Pattern Analysis and Machine Intelligence 27, 11 (2005): 1838-1842.
- [11] Pluempitiwiyawej, C., Moura, J. M. F., Wu., Y.-J. L., and Ho., C. STACS: New active contour scheme for cardiac MR image segmentation. IEEE Transaction on Medical Imaging 24, (2005): 593-603.
- [12] Li, C., Huang, R., Ding, Z., Gatenby, J. C., Metaxas, D. N., and Gore., J. C., A level set method for image segmentation in the presence of intensity inhomogeneities with application to MRI. IEEE Transaction on Image Processing 20, 7 (2011): 2007-2016.

- [13] Mumford, D., and Shah, J. Optimal approximation by piecewise smooth functions and associated variational problems. Communication on pure and applied mathematics 42 (1989): 577-658.
- [14] Tsai, A., Yezzi, A. and Willsky, A. S. Curve evolution implementation of the Mumford-Shah functional for image segmentation, denoising, interpolation, and magnification. IEEE Transaction on Image Processing 10, 8 (2001): 1169-1186.
- [15] Vese, L. A., and Chan., T. F. A multiphase level set framework for image segmentation using the Mumford and Shah model. International Journal of Computer Vision 50, 2 (2002): 271-293.
- [16] Zhao, H.-K., Chan, T. F., Merriman, B. and Osher., S. "A variational level set approach to multiphase motion. Journal of Computational Physics 127 (1996): 179-195.
- [17] Chan, T. F. and Vese, L. A. Active contours without edges. IEEE Transaction on Image Processing 50, 2 (2002): 271-293.
- [18] Yezzi, J. A., Tsai, A., and Willsky, A. A fully global approach to image segmentation via coupled curve evolution. Journal of Visual Communication and Image Representation 13, 1 (2002): 195-216.
- [19] Michailovich, O., Rathi, Y., and Tannenbaum, A. Image segmentation using active contours driven by the Bhattacharyya gradient flow. IEEE Transaction on Image Processing 16, 11 (2007): 2787-2801.
- [20] Bhattacharyya, A. On a measure of divergence between two statistical relations defined by their probabilities distribution. Bulletin Calcutta Mathematics Society 35 (1943): 99-109.
- [21] Li, C., Kao, C., Gore, J. C., and Ding, Z. Minimization of region-scalable fitting energy for image segmentation. IEEE Transaction on Image Processing 17, 10 (2008): 1940-1949.
- [22] Brox, T., and Cremers, D. On local region models and a statistical interpretation of the piecewise smooth Mumford-Shah functional. International Journal of Computer Vision 84, 1 (2008): 184-193.
- [23] Sum, K. W., and Cheung, P. Y. S. Vessel extraction under non-uniform illumination: A level set approach. IEEE Transaction on Biomedical Engineering 55, 1 (2008): 358-360.
- [24] Piovano, J., and Papadopoulos, T. Local statistics based region segmentation with automatic scale selection. Proceedings of the European Conference in Computer Vision (ECCV) 486-499, Marseille, France, 2008.

- [25] Lin, Y., Yang, Y., and Wang, X. A fast active contour model driven by global-local statistics energy." Proceedings of the Second International Symposium on International Intelligent Information Technology Application, 407-411. Shanghai, 2008.
- [26] Wang, L., He, L., Mishra, A., and Li, C. Active contours driven by local Gaussian distribution fitting energy. Signal Processing 89 (2009): 2435-2447.
- [27] Wang, L., Li, C., Sun, Q., Xia, D., and Kao, C-Y. Active contours driven by local and global intensity fitting energy with application brain MR image segmentation. Journal Medical Imaging and Graphics 33, 7 (2009): 520-531.
- [28] Zhang, K., Song, H. and Zhang, L. Active contours driven by local image fitting energy. Pattern Recognition 43, 4 (2010): 1199-1206.
- [29] Wang, X., Huang, G., and Xu, H. An efficient local Chan-Vese model for image segmentation. Pattern Recognition 43 (2010): 603-618.
- [30] Jung, M., Peyr'e, G., and Cohen, L. D. "Non-local active contour." Proceedings of the 3rd International Conference on Scale Space and Variational Models in Computer Vision (SSVM). Ein-Gedi, Israel, 2011.
- [31] Lankton, S., and Tannenbaum, A. Localizing region-based active contours. IEEE Transaction on Image Processing 17, 11 (2008): 2029-2039.
- [32] Darolti, C., Mertins, A., Bodensteiner, C., and Hofmann, U. G. Local region descriptor for active contours evolution. IEEE Transaction on Image Processing 17, 12 (2008): 2275-2288.
- [33] Phumeechanya, S., Pluempitiwiriyawej, C. and Thongvigitmanee, S. Active contour using local regional information on extendable search lines (LRES) for image segmentation. IEICE Transactions on Information and Systems E93-D, 6 (2010): 1625-1635.
- [34] Cootes, T. F., Taylor, C. J., Cooper, D. H., and Graham, J. Active shape models - their training and application. Computer Vision and Image Understanding 56, 3 (1995): 35-59.
- [35] Karaolani, P., Sullivan, G. D., and Baker, K. D. Active contours using finite element to control local scale. Proceedings of British Machine Vision Conference (BMVC), 481-487, 1992.
- [36] Ronfard, R. Region-based strategies for active contour models. International Journal of Computer Vision 3, 2 (1994): 229-251.
- [37] Mille, J. Narrow band region-based active contours and surfaces for 2D and 3D segmentation. Computer Vision and Image Understanding 113, 9 (2009): 946-965.

- [38] Li, H., and Yezzi, A. local or global minima: flexible dual-front active contours. IEEE Transaction on Pattern Analysis and Machine Intelligence 29, 1 (2007): 1-13.
- [39] Faisal, A., and Pluempitiwiriyaewj, C. Active contour using local region-scalable force with expandable kernel." Proceedings of IEEE International Conference on Information Science and Technology (ICIST). Wuhan, China, 2012.
- [40] Park, H., Schoepflin, T., and Kim, Y. Active contour model with gradient directional information: Directional snake. IEEE Transaction on Circuits and System for Video Technology 11, 2 (2001): 252-256.
- [41] Tang, J., S. Millington, Acton, S. T., Crandall, J., and Hurwitz, S. Surface extraction and thickness measurement of the articular cartilage from MR images using directional gradient vector flow snakes. IEEE Transaction on Biomedical Engineering 53, 5 (2006): 896-907.
- [42] Cheng, J., and Foo, S. W. Dynamic directional gradient vector flow for snakes. IEEE Transaction on Image Processing 15, 6 (2006): 1563-1571.
- [43] Phumeechanya, S., Pluempitiwiriyaewj, C., and Thongvigitmanee, S. Edge's type selectable active contour using local regional information on extendable search line." Proceedings 2010 IEEE International Conference on Image Processing (ICIP), 653-656. Hong Kong, 2010.
- [44] Faisal, A., and Pluempitiwiriyaewj, C. Directional local region-scalable active contour using expandable kernel." Proceedings 2012 9th International Conference on Electrical Engineering/Electronics, Computer, Telecommunications, and Information Technology (ECTI-CON). Hua Hin, Thailand, 2012.

APPENDICES

APPENDIX A

DERIVATION OF THE EQUATION

For convenience, we restate here our total energy function

$$E(\phi) = - \int_{\Omega} (\delta_{\epsilon}(\phi(\mathbf{y}))E_{\text{SLR}} - \nu|\nabla H_{\epsilon}(\phi(\mathbf{y}))|) d\mathbf{y} \quad (\text{A.1})$$

Since $H'_{\epsilon}(\phi) = \delta_{\epsilon}(\phi)$, we get $H_{\epsilon}(\phi) = \delta_{\epsilon}(\phi)|\nabla\phi|$. Thus, by substituting E_{SLR} with (3.6), E becomes

$$E(\phi) = - \int_{\Omega} \left(\delta_{\epsilon}(\phi(\mathbf{y})) \int_{\Omega} K(\mathbf{x} - \mathbf{y}) \cdot F(I(\mathbf{x}), \phi(\mathbf{x})) d\mathbf{x} - \nu\delta_{\epsilon}(\phi(\mathbf{y}))|\nabla\phi(\mathbf{y})| \right) d\mathbf{y} \quad (\text{A.2})$$

To obtain the optimal ϕ , the first variation the Euler-Lagrange equations for the level set must be taken. To compute the variation of ϕ , we consider replacing ϕ with $\phi + \xi\psi$ where ψ represents a tiny change perpendicular to ϕ weighted by a small number ξ . We change the parameters by writing $E(\phi)$ as $E(\phi + \xi\psi)$

$$E(\phi + \xi\psi) = - \left(\int_{\Omega} \delta_{\epsilon}(\phi(\mathbf{y}) + \xi\psi) \int_{\Omega} K(\mathbf{x} - \mathbf{y}) \cdot F(I(\mathbf{x}), \phi(\mathbf{x}) + \xi\psi) d\mathbf{x} d\mathbf{y} - \nu \int_{\Omega} \delta_{\epsilon}(\phi(\mathbf{y}) + \xi\psi)|\nabla(\phi(\mathbf{y}) + \xi\psi)| d\mathbf{y} \right) \quad (\text{A.3})$$

Since E is minimized by ϕ , the partial derivative of this energy is derived with respect to ξ , $\frac{\partial E(\phi + \xi\psi)}{\partial \xi} = 0$, evaluated at $\xi = 0$ to represent a small differential of movement.

$$\begin{aligned} \frac{\partial E(\phi + \xi\psi)}{\partial \xi} \Big|_{\xi=0} &= - \left(\int_{\Omega} \delta_{\epsilon}(\phi(\mathbf{y})) \times \int_{\Omega} \psi K(\mathbf{x} - \mathbf{y}) \frac{\partial F(I(\mathbf{x}), \phi(\mathbf{x}))}{\partial \phi(\mathbf{x})} d\mathbf{x} d\mathbf{y} \right. \\ &\quad + \psi \int_{\Omega} \delta'_{\epsilon}(\phi(\mathbf{y})) \int_{\Omega} K(\mathbf{x} - \mathbf{y}) \cdot F(I(\mathbf{x}), \phi(\mathbf{x})) d\mathbf{x} d\mathbf{y} \\ &\quad \left. - \nu \int_{\Omega} \left(\delta'_{\epsilon}(\phi(\mathbf{y}))|\nabla\phi(\mathbf{y})|\psi + \delta_{\epsilon}(\phi(\mathbf{y})) \frac{\partial |\nabla(\phi(\mathbf{y}) + \xi\psi)|}{\partial \xi} \right) d\mathbf{y} \right) \end{aligned} \quad (\text{A.4})$$

The last partial derivative of the third term in (A.4) is expressed by plugging in $\xi = 0$.

$$\begin{aligned} \frac{\partial |\nabla(\phi(\mathbf{y}) + \xi\psi)|}{\partial \xi} &= \frac{1}{2|\nabla(\phi(\mathbf{y}) + \xi\psi)|} + \frac{\partial}{\partial \xi} \left(\left(\frac{\partial \phi(\mathbf{y})}{\partial x} + \xi \frac{\partial \psi}{\partial x} \right)^2 + \left(\frac{\partial \phi(\mathbf{y})}{\partial y} + \xi \frac{\partial \psi}{\partial y} \right)^2 \right) \\ &= \frac{1}{2|\nabla(\phi(\mathbf{y}))|^2} \left(\frac{\partial \phi(\mathbf{y})}{\partial x} \frac{\partial \psi}{\partial x} + \frac{\partial \phi(\mathbf{y})}{\partial y} \frac{\partial \psi}{\partial y} \right) = \frac{\nabla\phi(\mathbf{y})\nabla\psi}{|\nabla\phi(\mathbf{y})|} \end{aligned} \quad (\text{A.5})$$

On the zero level set function, $\delta'_{\epsilon}(\phi(\mathbf{y}))$ in the third term of (A.4) evaluates to zero. So, the

contour movement is not affected and this term can be ignored. By plugging in the term in (A.5) into the last partial derivative of the first term in (A.4) and integrating it by parts, we obtain

$$\begin{aligned}
\frac{\partial E(\phi + \xi\psi)}{\partial \xi} \Big|_{\xi=0} &= - \left(\int_{\Omega} \int_{\Omega} \psi \delta_{\epsilon}(\phi(\mathbf{y})) K(\mathbf{x} - \mathbf{y}) \times \frac{\partial F(I(\mathbf{x}), \phi(\mathbf{x}))}{\partial \phi(\mathbf{x})} d\mathbf{x} d\mathbf{y} \right. \\
&\quad \left. - \nu \int_{\Omega} \left(\delta'_{\epsilon}(\phi(\mathbf{y})) |\nabla \phi(\mathbf{y})| \psi + \delta_{\epsilon}(\phi(\mathbf{y})) \frac{\nabla \phi(\mathbf{y}) \nabla \psi}{|\nabla \phi(\mathbf{y})|} \right) d\mathbf{y} \right) \\
&= - \left(\int_{\Omega} \int_{\Omega} \psi \delta_{\epsilon}(\phi(\mathbf{y})) K(\mathbf{x} - \mathbf{y}) \times \frac{\partial F(I(\mathbf{x}), \phi(\mathbf{x}))}{\partial \phi(\mathbf{x})} d\mathbf{x} d\mathbf{y} \right. \\
&\quad \left. - \nu \int_{\Omega} \left(\delta'_{\epsilon}(\phi(\mathbf{y})) |\nabla \phi(\mathbf{y})| \psi - \operatorname{div} \left(\delta_{\epsilon}(\phi(\mathbf{y})) \frac{\nabla \phi(\mathbf{y})}{|\nabla \phi(\mathbf{y})|} \right) \psi \right) d\mathbf{y} \right) \\
&\quad + \int_{\partial \Omega} \frac{\delta_{\epsilon}(\phi(\mathbf{y}))}{|\nabla \phi(\mathbf{y})|} \nabla \phi(\mathbf{y}) \vec{n} \psi d\mathbf{y} \tag{A.6}
\end{aligned}$$

where \vec{n} denotes the exterior normal to the boundary $\partial \Omega$. We can write

$$\begin{aligned}
\operatorname{div} \left(\delta_{\epsilon}(\phi(\mathbf{y})) \frac{\nabla \phi(\mathbf{y})}{|\nabla \phi(\mathbf{y})|} \right) &= \frac{\partial}{\partial x} \left(\delta_{\epsilon}(\phi(\mathbf{y})) \frac{\phi_x(\mathbf{y})}{|\nabla \phi(\mathbf{y})|} \right) + \frac{\partial}{\partial y} \left(\delta_{\epsilon}(\phi(\mathbf{y})) \frac{\phi_y(\mathbf{y})}{|\nabla \phi(\mathbf{y})|} \right) \\
&= \delta'_{\epsilon}(\phi(\mathbf{y})) \frac{\phi_x^2(\mathbf{y})}{|\nabla \phi(\mathbf{y})|} + \delta_{\epsilon}(\phi(\mathbf{y})) \frac{\partial}{\partial x} \left(\frac{\nabla \phi(\mathbf{y})}{|\nabla \phi(\mathbf{y})|} \right) \\
&\quad + \delta'_{\epsilon}(\phi(\mathbf{y})) \frac{\phi_y^2(\mathbf{y})}{|\nabla \phi(\mathbf{y})|} + \delta_{\epsilon}(\phi(\mathbf{y})) \frac{\partial}{\partial y} \left(\frac{\nabla \phi(\mathbf{y})}{|\nabla \phi(\mathbf{y})|} \right) \\
&= \delta'_{\epsilon}(\phi(\mathbf{y})) |\nabla \phi(\mathbf{y})| + \delta_{\epsilon}(\phi(\mathbf{y})) \operatorname{div} \left(\frac{\nabla \phi(\mathbf{y})}{|\nabla \phi(\mathbf{y})|} \right) \tag{A.7}
\end{aligned}$$

By plugging in (A.7) to the first term of (A.6)

$$\begin{aligned}
\left(\frac{\partial E}{\partial \phi}, \psi \right) &= - \int_{\Omega} \left(\int_{\Omega} \delta_{\epsilon}(\phi(\mathbf{y})) K(\mathbf{x} - \mathbf{y}) \times \frac{\partial F(I(\mathbf{x}), \phi(\mathbf{x}))}{\partial \phi(\mathbf{x})} d\mathbf{x} \right. \\
&\quad \left. + \nu \left(\delta_{\epsilon}(\phi(\mathbf{y})) \operatorname{div} \left(\frac{\nabla \phi(\mathbf{y})}{|\nabla \phi(\mathbf{y})|} \right) \right) \right) \psi d\mathbf{y} + \nu \int_{\partial \Omega} \frac{\delta_{\epsilon}(\phi(\mathbf{y}))}{|\nabla \phi(\mathbf{y})|} \nabla \phi(\mathbf{y}) \vec{n} \psi d\mathbf{y} \tag{A.8}
\end{aligned}$$

According to the chain rule, the partial derivative in (A.6) can be written by simultaneously plugging in $\xi = 0$ thus achieving $\frac{\partial E}{\partial \phi}$. For all ψ , this partial derivative must be zero, then, we have $\frac{\partial E}{\partial \phi} = 0$. The Cauchy-Schwartz inequality can be used to show the optimal direction to move ϕ . Hence, the gradient flow equation is expressed as

$$\begin{aligned}
\frac{\partial \phi}{\partial t} &= \delta_{\epsilon}(\phi(\mathbf{y})) \int_{\Omega} K(\mathbf{x} - \mathbf{y}) \frac{\partial F(I(\mathbf{x}), \phi(\mathbf{x}))}{\partial \phi(\mathbf{x})} d\mathbf{x} + \nu \delta_{\epsilon}(\phi(\mathbf{y})) \operatorname{div} \left(\frac{\nabla \phi}{|\nabla \phi|} \right) \\
&= \delta_{\epsilon}(\phi(\mathbf{y})) \left(\int_{\Omega} K(\mathbf{x} - \mathbf{y}) \frac{\partial F(I(\mathbf{x}), \phi(\mathbf{x}))}{\partial \phi(\mathbf{x})} d\mathbf{x} + \nu \operatorname{div} \left(\frac{\nabla \phi(\mathbf{y})}{|\nabla \phi(\mathbf{y})|} \right) \right) \\
&= \delta_{\epsilon}(\phi(\mathbf{y})) (F_{\text{SLR}} + F_{\text{SM}}) \tag{A.9}
\end{aligned}$$

with initial condition $\phi(\mathbf{y}, 0) = \phi_0(\mathbf{y})$, $(\mathbf{y}) \in \mathbb{R}$ and boundary condition $\frac{\delta_{\epsilon}(\phi)}{|\nabla \phi|} \frac{\partial \phi}{\partial \vec{n}} = 0$ on $\partial \Omega$, where $\frac{\partial \phi}{\partial \vec{n}}$ denotes the normal derivative of ϕ at the boundary.

APPENDIX B

LIST OF PUBLICATIONS

Parts of this work are published in the following articles.

International Conference Proceedings

1. Amir Faisal and Charnchai Pluempitiwiriyawej, "Active Contour Using Local Region-Scalable Force With Expandable Kernel", Proceedings of 2012 IEEE International Conference on Information Science and Technology (ICIST), pp. 18-24, Wuhan, Hubei, China, March 23-25, 2012.
2. Amir Faisal and Charnchai Pluempitiwiriyawej, "Directional Local Region-Scalable Active Contour Using Expandable Kernel", Proceedings of 2012 9th International Conference on Electrical Engineering/Electronics, Computer, Telecommunications, and Information Technology (ECTI-CON), Hua Hin, Thailand, May 16-18, 2012.

Biography

Amir Faisal was born on October 3rd, 1988 in Sukabumi, Indonesia. In 2005-2009, he studied Engineering Physics in Universitas Gadjah Mada, Yogyakarta, Indonesia. In 2010-2012, he achieved the JICA - AUN/SEED-Net Scholarship and enrolled in master's program of Electrical Engineering in Chulalongkorn University (CU), Bangkok, Thailand. He performed research on image segmentation using active contour models at the Digital Signal Processing Research Laboratory in CU under supervision of Assistant Professor Charnchai Pluempitiwiriyaewj. His research interest includes Active Contour Models or Level Set Methods.